HHS Public Access

Author manuscript

Cell Rep. Author manuscript; available in PMC 2025 May 14.

Published in final edited form as:

Cell Rep. 2025 April 22; 44(4): 115539. doi:10.1016/j.celrep.2025.115539.

TFE3 fusion oncoprotein condensates drive transcriptional reprogramming and cancer progression in translocation renal cell carcinoma

Choon Leng So[1,6], **Ye Jin Lee**[1,6], **Bujamin H. Vokshi**[2,6], **Wanlu Chen**[2,3], **Binglin Huang**[1], **Emily De Sousa**[1], **Yangzhenyu Gao**[3], **Marie Elena Portuallo**[1], **Sumaiya Begum**[1], **Kasturee Jagirdar**[1], **W. Marston Linehan**[4], **Vito W. Rebecca**[1,2], **Hongkai Ji**[3], **Eneda Toska**[1,2,*], **Danfeng Cai**[1,2,5,7,8,*]

[1]Department of Biochemistry and Molecular Biology, Johns Hopkins Bloomberg School of Public Health, Baltimore, MD 21205, USA

[2]Department of Oncology, Johns Hopkins School of Medicine, Baltimore, MD 21205, USA

[3]Department of Biostatistics, Johns Hopkins Bloomberg School of Public Health, Baltimore, MD 21205, USA

[4]Urologic Oncology Branch, National Cancer Institute, Bethesda, MD 20892, USA

[5]Department of Biophysics and Biophysical Chemistry, Johns Hopkins School of Medicine, Baltimore, MD 21205, USA

[6]These authors contributed equally

[7]X (formerly Twitter): @DanfengCai

*Correspondence: etoska1@jhmi.edu (E.T.), danfeng.cai@jhu.edu (D.C.).

AUTHOR CONTRIBUTIONS

Conceptualization, C.L.S., Y.J.L., B.H.V., D.C., and E.T.; methodology, C.L.S., Y.J.L., B.H.V., and B.H.; formal analysis, C.L.S., Y.J.L., B.H.V., W.C., and Y.G.; investigation, C.L.S., Y.J.L., B.H.V., W.C., B.H., E.D.S., and Y.G.; resources, M.E.P., S.B., K.J., V.R., and W.M.L.; writing – original draft, C.L.S., Y.J.L., B.H.V., D.C., and E.T.; writing – review & editing, C.L.S., Y.J.L., B.H.V., W.M.L., D.C., and E.T.; funding acquisition, W.M.L., V.W.R., H.J., D.C., and E.T.; supervision, V.W.R., H.J., D.C., and E.T.

DECLARATION OF INTERESTS

E.T. reports grants from Astrazeneca and consulting fees from Astrazeneca and Menarini.

RESOURCE AVAILABILITY

Lead contact

Further information and requests for resources and reagents should be directed to and will be fulfilled by the lead contact, Danfeng Cai (danfeng.cai@jhu.edu).

Materials availability

All materials generated in this study are available upon request.

Data and code availability

- The RNA-seq, ATAC-seq, and CUT&RUN fastq data and processed files are available at GEO: GSE281165. Microscopy data reported in this paper will be shared by the lead contact upon request.
- Custom codes are included as supplemental information. Other codes are available from the lead contact upon request.
- Any additional information required to reanalyze the data reported in this paper is available from the lead contact upon request.

SUPPLEMENTAL INFORMATION

Supplemental information can be found online at https://doi.org/10.1016/j.celrep.2025.115539.

[8]Lead contact

SUMMARY

Translocation renal cell carcinoma (tRCC) presents a significant clinical challenge due to its aggressiveness and limited treatment options. It is primarily driven by fusion oncoproteins (FOs), yet their role in oncogenesis is not fully understood. Here, we investigate TFE3 fusions in tRCC, focusing on NONO::TFE3 and SFPQ::TFE3. We demonstrate that TFE3 FOs form liquid-like condensates with increased transcriptional activity, localizing to TFE3 target genes and promoting cell proliferation and migration. The coiled-coil domains (CCDs) of NONO and SFPQ are essential for condensate formation, prolonging TFE3 FOs' chromatin binding time and enhancing transcription. Compared with wild-type TFE3, TFE3 FOs bind to new chromatin regions, alter chromatin accessibility, and form new enhancers and super-enhancers at pro-growth gene loci. Disruption of condensate formation via CCD modification abolishes these genome-wide changes. Altogether, our integrated analyses underscore the critical functions of TFE3 FO condensates in driving tumor cell growth, providing key insights for future therapeutic strategies.

Graphical Abstract

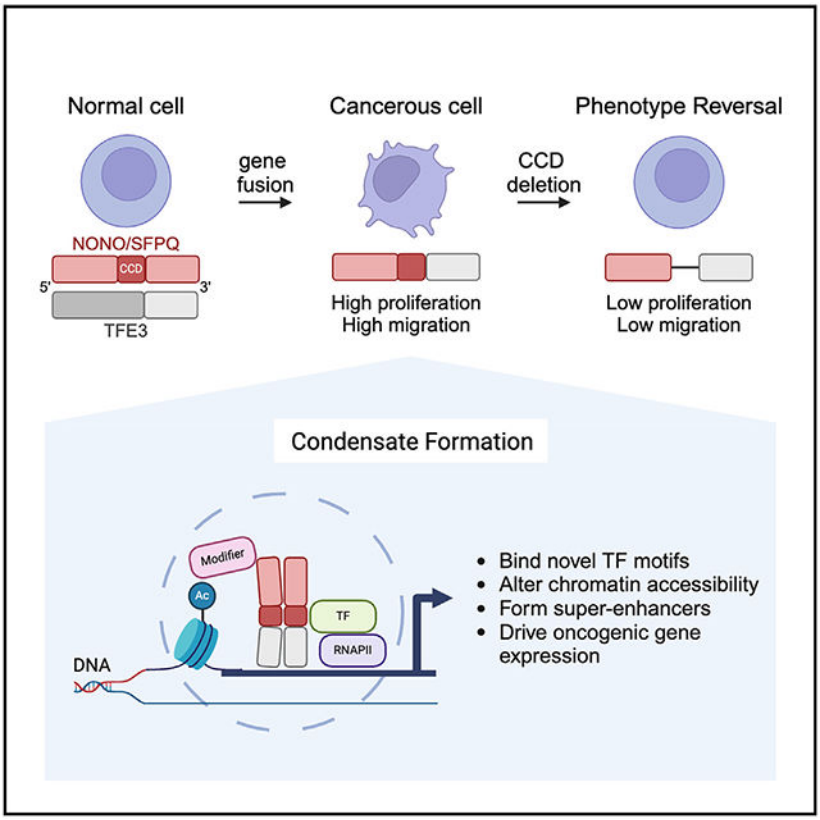

In brief

So et al. investigate TFE3 fusion oncoproteins (FOs) in translocation renal cell carcinoma (tRCC) and find that TFE3 FOs form transcriptional condensates and drive tRCC progression. The

structured coiled-coil domain of TFE3 FOs is essential for condensate formation, prolonging TFE3 FOs' chromatin binding time and enhancing oncogenic transcription.

INTRODUCTION

Translocation renal cell carcinoma (tRCC) is an aggressive form of renal cell carcinoma (RCC) that has the predisposition to spread when the primary tumor is small and, currently, there is no specific treatment option available.[1] Although rare, it is responsible for over 40% of renal carcinomas (RCCs) in children and young adults.[2] tRCCs are driven by chromosomal rearrangements involving the microphthalmia-associated transcriptional factor (TF) family with TF binding to IGHM enhancer 3 (TFE3) being the most common.[1] These TFs use helix-loop-helix leucine zipper domains to dimerize and bind to E-box sequences and regulate the expression of genes important in lysosome biogenesis and metabolism.[1] In TFE3 fusions, the C-terminal DNA-binding domain of TFE3 is retained, while the N-terminal region is replaced with distinct fusion partners known thus far with PRCC (papillary RCC), NONO (non-POU domain containing, octamer binding) and SFPQ (splicing factor proline/glutamine-rich) being the most frequent.[1,3] Since the initial discovery of PRCC::TFE3 fusion nearly three decades ago,[4,5] our understanding of how TFE3 fusion oncoproteins (FOs) drive tRCC remains limited.[6] While there have been recent genomics and transcriptomics studies of TFE3 FOs,[7-9] the molecular mechanisms of how TFE3 FOs drive oncogenesis are largely unknown, hindering therapy development.

Biomolecular condensates are membrane-less compartments inside cells formed by weak, multivalent interactions among macromolecules.[10] Without the need for extra energy, biomolecular condensates concentrate specific molecules to accelerate reactions, buffer molecules outside the condensates, or inactivate reactions by excluding molecules from reaction centers.[11] It has been reported that FOs are prone to forming biomolecular condensates.[12-15] While the intrinsically disordered regions within FOs are known to drive condensate formation, the contributions of many structured domains in this process are unclear. Recently a study suggested that a specific TFE3 FO, NONO::TFE3 can form biomolecular condensates.[16] While condensate formation is presumed to promote NONO::TFE3 stability,[16] its role in transcription and chromatin regulation is unknown, and whether condensate formation is a feature of other TFE3 FOs is unclear.

In this work, we focus on two common TFE3 FOs, NONO::TFE3 and SFPQ::TFE3, which constitute 30%–40% of all TFE3 FOs.[1,3] In these fusions, exons 1–5 of TFE3 are replaced with the N-terminal domains of either NONO or SFPQ (Figure 1A), both are RNA-binding proteins belonging to the Drosophila Biology Human Splicing (DBHS) family.[17] We found that NONO::TFE3 and SFPQ::TFE3 FOs form biomolecular condensates in patient-derived cell lines, patient tumor tissue, and xenograft models. Notably, TFE3 FOs condensate formation is mediated by the helical coiled-coil domain (CCD) within NONO and SFPQ. By forming condensates, TFE3 FOs can associate with RNA polymerase II (Pol II) and active chromatin marks, and alter canonical TFE3 genome binding, which drives a remodeling of the chromatin landscape ultimately promoting TFE3 tRCC proliferation and migration. This

study reveals a key mechanism for TFE3 FOs to drive cancer, providing the foundation for the development of targeted therapies against TFE3 fusion condensates.

RESULTS

TFE3 FOs form biomolecular condensates in patient cell lines and tissue

To test if TFE3 FOs form biomolecular condensates, we expressed wild-type TFE3, NONO::TFE3, and SFPQ::TFE3 each attached to enhanced GFP (eGFP) in the U-2 OS cell line. We found that, compared with TFE3, which is diffuse in both the cytoplasm and the nucleus, TFE3 FOs predominantly localize to the nucleus and form distinct, round foci resembling liquid-like condensates (Figures 1B and 1C). Using cell mean intensity as a proxy for protein expression level, we found that NONO::TFE3::eGFP and SFPQ::TFE3::eGFP form foci at lower concentrations than TFE3 and in a concentration-dependent manner (Figure 1D). These findings indicate that TFE3 FOs gained abilities to phase separate and form foci. To understand if endogenous TFE3 FOs form condensates in the patient-derived cell lines, we examined NONO::TFE3 organization in UOK109 and SFPQ::TFE3 organization in UOK145, both patient-derived tRCC cell lines harboring these respective TFE3 FOs.[18,19] Consistent with the U-2 OS data, we found that endogenous TFE3 FOs organized into distinct nuclear foci in UOK109 and UOK145 cells (Figure 1E, right). On the contrary, wild-type TFE3 in HK2 (normal renal tubular cells), ACHN (human renal adenocarcinoma cells), and U-2 OS cells was diffuse and formed few foci (Figures 1E, left, and S1A, left). Three-dimensional (3D) tissue can differ from cultured cells in tissue mechanics and secreted factors in the extracellular matrix.[20] To confirm that TFE3 FOs also form foci in tissue, we performed immunofluorescence (IF) on SFPQ::TFE3 patient samples and found that while the normal patient tissue expressing wild-type TFE3 showed low, cytoplasmic, and nuclear expression of TFE3, the tumor tissue showed predominantly nuclear expression of SFPQ::TFE3 organized into distinct puncta/condensates (Figures 1F, top, and S1B). Since NONO::TFE3 patient tumor is unavailable, we made a mouse xenograft tumor of UOK109 to examine NONO::TFE3 organization in tissue. Similar to SFPQ::TFE3, NONO::TFE3 in the mouse xenograft tumor also organized into prominent nuclear puncta/condensates (Figure 1G). Foci formation appears to be a general property of TFE3 FOs, since two other common TFE3 FOs, ASPSCR1::TFE3 and PRCC::TFE3 both form foci in patient-derived cell lines (Figure S1A, right) and in patient tumors (Figure 1F, bottom). These results show that, distinct from wild-type TFE3, TFE3 FOs form condensates in cells and tumors.

To investigate if TFE3 FO condensates are liquid-like, we used fluorescence recovery after photobleaching (FRAP) to examine the dynamics of NONO::TFE3::eGFP in a UOK109 CRISPR knockin (KI) cell line, in which the endogenous NONO::TFE3 was labeled with eGFP (Figures S1C-S1E). NONO::TFE3::eGFP forms clear nuclear foci in the UOK109 KI similar to endogenous ones (Figure S1E), and recovered fluorescence rapidly after FRAP (Figure 1H; Video S1) with a half-time of fluorescence recovery $t_{1/2}$ of 8.9 s. Similarly, the condensates formed by both NONO::TFE3::eGFP and SFPQ::TFE3::eGFP were dynamic when expressed in the HEK293T cell line (Figure S1F; Videos S2 and S3) and recovered after FRAP with a $t_{1/2}$ of 11.9 and 13.3 s, respectively. Consistent with the FRAP results,

we found that NONO::TFE3::eGFP in the UOK109 KI cells can be rapidly dissolved by 1,6-hexanediol (an aliphatic alcohol that disrupts transient bonds within a condensate[21]) (Figure 1I; Videos S4 and S5). Additionally, condensate fusion and fission events were also observed (Figures 1J and 1K; Videos S6 and S7), although most condensates are stationary possibly due to anchorage to the chromatin. These results indicate that the condensates formed by NONO::TFE3 and SFPQ::TFE3 are dynamic and liquid-like.

TFE3 FO condensates are associated with active transcription

To test if TFE3 FO condensates are associated with active transcription, we probed their colocalization with active transcription markers in the patient-derived cell lines UOK109 and UOK145. Specifically, RNA polymerase II (Pol II) is the transcription machinery for most messenger RNAs,[22] bromodomain-containing protein 4 (BRD4) is a co-activator that localizes to active genes,[23] and histone H3 lysine 27 acetylation (H3K27ac) is a histone modification of enhancers.[24] We found that NONO::TFE3 and SFPQ::TFE3 have higher colocalization with RNA Pol II, BRD4, and H3K27ac in the patient-derived cells compared with TFE3 in HK2 cells (Figures 2A and 2B), indicating that TFE3 FO condensates can more extensively associate with transcription-related factors than TFE3. Interestingly, NONO::TFE3 and SFPQ::TFE3 condensates colocalize more to the RNA Pol IIs that are initiating (RNA Pol II pSer5) than those that are elongating (RNA Pol II pSer2)[25] (Figures S2A and S2B), indicating that TFE3 FO condensates mainly mediate transcription initiation. On the other hand, TFE3 FO condensates do not colocalize with a heterochromatin marker histone 3 lysine 9 trimethylation (H3K9me3) (Figures 2A and 2B). These results indicate that condensates formed by NONO::TFE3 and SFPQ::TFE3 are associated with active transcription.

To test if NONO::TFE3 and SFPQ::TFE3 condensates are transcribing their target genes, we investigated their relations with two well-known target genes *GPNMB* (glycoprotein nonmetastatic melanoma B) and *NMRK2* (nicotinamide ribokinase 2),[6,26-30] and a new target gene *RTN4RL2* (reticulon 4 receptor-like 2, identified in our integrated RNA-seq and CUT&RUN data). NONO::TFE3 and SFPQ::TFE3 were more capable of transcribing these target genes compared with TFE3 (Figure 2C). Importantly, the high transcription activity of TFE3 FOs was mediated through the condensates they formed, as TFE3 FO condensates concentrated at *GPNMB* transcription sites (Figures 2D and 2E). On the contrary, we did not see TFE3 concentrating at *GPNMB* in HK2 cells as HK2 had low *GPNMB* expression (Figure 2C) and did not have visible *GPNMB* transcription sites (Figure 2D). As negative controls, both TFE3 FOs and wild-type TFE3 were excluded from sites of the housekeeping gene *ACTB* that encodes β-actin (Figures 2D and 2E). These results show that TFE3 FO condensates can regulate TFE3-dependent transcription.

The CCD is important for condensate formation and transcriptional functions

Next, we investigated the molecular basis of NONO::TFE3 and SFPQ::TFE3 condensate formation. NONO and SFPQ share similar domain organizations[17] (Figure 1A) and we postulated that the domains in NONO and SFPQ promote TFE3 FO condensate formation. To test this, we created constructs with deletions of the prion-like domain (PLD), RNA recognition domain 1 (RRM1), RNA recognition domain 2 (RRM2), both RRMs and

the CCD in NONO::TFE3 and SFPQ::TFE3, respectively (Figure 3A), fused them to eGFP, and expressed them in U-2 OS cells. We found that, while NONO::TFE3::eGFP forms condensates in a concentration-dependent manner (Figures 3B-3D), deleting its CCD dramatically decreased its ability to form condensates, similar to that of wild-type TFE3 (Figures 3B-3D). Interestingly, deleting the PLD, a domain promoting condensate formation in other proteins such as FUS and EWSR1[31,32] did not affect NONO::TFE3::eGFP condensate formation, while deleting RRM1 and RRM2 had milder effects on condensate formation compared with deleting CCD (Figures 3B-3D). These results show that CCD is essential for NONO::TFE3 condensate formation. Similar to NONO::TFE3, deleting CCD in SFPQ::TFE3 most significantly decreased condensate formation, while deleting PLD mildly decreased SFPQ::TFE3 condensate formation, and deleting RRMs, specifically RRM2, had strong effects on condensate formation (Figures 3B-3D). These results indicate that, while CCDs are essential for condensate formation in both NONO::TFE3 and SFPQ::TFE3, other domains have varying effects on condensate formation in the two TFE3 FOs, likely due to the inherent molecular differences in the two TFE3 FOs.[1,3] To characterize the CCD interactions, we mutated the highly conserved hydrophobic a and d residues on the coiled-coil interaction surface to alanine (Figures 3A and 3E, NONOmut::TFE3 and SFPQmut::TFE3), which are known to disrupt the interaction of SFPQ with other DBHS family proteins.[33] We found that NONOmut::TFE3 partitioned less to the condensates compared with NONO::TFE3 (Figures 3B and 3F), and SFPQmut::TFE3 formed fewer condensates compared with SFPQ::TFE3 (Figures 3B and 3G), albeit not as drastic as their ΔCCD counterparts (Figures 3F and 3G). Therefore, specific CCD interactions are important for forming TFE3 FOs condensates.

After confirming the key role of CCDs, we examined their sufficiency in condensate formation, we conducted optogenetics experiments using optoDroplet, which uses Cry2WT to assess the ability of protein domains to form condensates in response to blue light[34] (Figure S3A). Consistent with previous studies,[34] we observed that, after light activation, Cry2WT alone did not form optoDroplets. In contrast, fusing well-known condensate-forming domains such as TDP-$43_{274\text{-}414}$ and $FUS_{1\text{-}214}$[35,36] to Cry2WT increased optoDroplet formation (Figure S3B). Confirming our findings that the CCD is important for TFE3 FO condensate formation, we found that CCD of NONO effectively promoted optoDroplet formation with light activation (Figures S3C and S3D). While the CCD of SFPQ alone was insufficient for optoDroplet formation, further including the disordered region after CCD (CCD-IDR) promoted optoDroplet formation (Figures S3C and S3E), again demonstrating slight differences between the two homologous fusion partners of TFE3 FOs. Fusing PLD and RRM1 of NONO and SFPQ to Cry2WT did not promote optoDroplet formation with photoactivation but fusing RRM2 did (Figures S3C-S3E), which largely agrees with our studies in expressing various domain deletion TFE3 FOs in U-2 OS cells. Overall, we found that the CCDs of NONO and SFPQ are necessary and important for TFE3 FO condensate formation.

To investigate if condensate formation is necessary for the transcriptional functions of NONO::TFE3 and SFPQ::TFE3, we compared the *GPNMB* mRNA levels in U-2 OS cells expressing wild-type TFE3, TFE3 FOs, and various domain deletion and CCD mutants of TFE3 FOs. Consistent with the notion that condensate formation

is necessary for the transcriptional activities of TFE3 FOs, we found that deleting CCD in both NONO::TFE3 and SFPQ::TFE3, which abolished TFE3 FO condensates formation, significantly decreased TFE3 target gene *GPNMB* expression (Figure 3H). Further confirming the link between condensate formation and transcriptional activity, NONOΔPLD::TFE3, which forms as many condensates as NONO::TFE3 (Figures 3B-3D), expresses a similar level of *GPNMB* to NONO::TFE3 (Figure 3H). In contrast, SFPQΔPLD::TFE3, which forms fewer condensates than SFPQ::TFE3 (Figures 3B-3D), expresses lower *GPNMB* than SFPQ::TFE3. While not statistically significant, both NONOmut::TFE3 and SFPQmut::TFE3 showed lower *GPNMB* expression than the TFE3 FOs, similar to the ΔCCD mutants (Figure 3H). The higher *GPNMB* expression in CCDmut (compared with ΔCCD) could be attributed to the higher foci count, demonstrating the link between condensate formation and transcriptional activity. On the other hand, RRM deletions have varying effects on *GPNMB* expression, possibly due to the compensatory effects after RRM deletions. Nevertheless, there is an overall strong positive correlation between foci number and *GPNMB* expression in various cells expressing full-length and mutant constructs (except RRM deletions in SFPQ::TFE3) (Figure 3I), demonstrating that the ability of TFE3 FOs to form condensates is linked to their transcriptional activities.

Lastly, we investigated whether condensate formation is sufficient for the transcriptional functions of TFE3 FOs. To this end, we replaced the CCD or the entire N-terminal fusion partner of TFE3 with other domains known to promote condensate formation and created three synthetic TFE3 fusions: a construct with CCD directly fused to TFE3 ((NONO)CCD::TFE3), a NONO::TFE3 with CCD replaced with TDP-$43_{274\text{-}424}$ (NONO::TDP-43::TFE3), and a construct with $FUS_{1\text{-}267}$ fused to TFE3 (FUS::TFE3) (Figure S3F). Among these constructs, (NONO)CCD::TFE3 and FUS::TFE3 formed condensates, while NONO::TDP-43::TFE3 did not (Figures S3G-S3I). While TDP-43 failed to recapitulate CCD-mediated protein interactions and *GPNMB* expression in NONO::TFE3, (NONO)CCD::TFE3 and FUS::TFE3 significantly elevated *GPNMB* expression (Figure S3J), consistent with the importance of condensate formation in driving TFE3 FO target gene expression. Together, these results indicate that condensate formation is sufficient for the transcription activities of TFE3 FOs.

TFE3 FO condensates mediate TFE3 tRCC proliferation and migration

TFE3 tRCC is an aggressive cancer with metastasis common at diagnosis and no effective treatments.[1] To understand how condensate formation affects tRCC cell proliferation and migration, we used CRISPR-Cas9 to knock out NONO::TFE3 in the UOK109 cells (UOK109 KO) (Figures 4A and S4A), and made stable cell lines rescued with TFE3 ($TFE3^R$), NONO::TFE3 ($NONO::TFE3^R$), NONOΔCCD::TFE3 ($NONOΔCCD::TFE3^R$) or NONOmut::TFE3 ($NONOmut::TFE3^R$) (Figures 4A and S4B). We also made stable rescue cell lines of SFPQ::TFE3 ($SFPQ::TFE3^R$) and SFPQΔCCD::TFE3 ($SFPQΔCCD::TFE3^R$) in UOK109 KO, as we could not KO SFPQ::TFE3 in UOK145 cells (Figures 4A and S4B). These proteins were fused to the HaloTag and 3xFLAG Tag to facilitate live-cell imaging and genomics experiments. We first confirmed that the reintroduced proteins in these cell lines had similar expression levels, and were close to that of the endogenous NONO::TFE3 in UOK109 cells without significant protein degradation (Figure S4B). Consistent with

those in U-2 OS cells, NONO::TFE3 and SFPQ::TFE3 were nuclear and punctate in the rescue cells, the ΔCCD and CCDmut were nuclear but diffused, and wild-type TFE3 mainly localized to the cytoplasm (Figures 4B and 4C), indicating that CCDs mediate NONO::TFE3 and SFPQ::TFE3 condensate formation in patient-derived cell lines and possibly through increased valency via homo-/hetero-dimerization with SFPQ and PSPC1 (paraspeckle component 1, another member of the DBHS protein family[33]) (Figure S4C). CCDs are also important for NONO::TFE3 and SFPQ::TFE3 transcription activities in patient-derived cell lines, as NONO::TFE3^{R} and SFPQ::TFE3^{R} increased the expression of target genes compared with UOK109 KO cell lines, while NONOΔCCD::TFE3^{R} and SFPQΔCCD::TFE3^{R} blunted these increases (Figures 4D and S4D).

Using these rescue cell lines, we examined whether TFE3 FO condensates drive cell growth. We first noticed that different rescue cell lines have distinct cellular morphology, hinting at their different transcription programs (Figures 4E and 4F). We then assessed cell proliferation by detecting DNA synthesis through 5-ethynyl 2′-deoxyuridine incorporation. We found that cells expressing full-length TFE3 FOs proliferated faster compared with KO cells, cells expressing their ΔCCD counterparts, and cells expressing TFE3 (Figures 4G and 4H), indicating that TFE3 FO condensates promote cell proliferation. Next, we assessed cell migration through a scratch wound assay and found that cells expressing full-length TFE3 FOs migrated faster than KO, wildtype TFE3, and their ΔCCD counterparts (Figures 4I-4K). Specifically, wound closure occurred at ~15 h for cells expressing full-length TFE3 FOs, while KO, wild-type TFE3, and ΔCCD rescue cells required 24 h or longer (Figure 4J). To verify that the effect of TFE3 FO condensates on cancer is not limited to specific cell lines, we made orthogonal T-REx 293 doxycycline-inducible cell lines to compare the effects of TFE3, SFPQ::TFE3, and SFPQΔCCD::TFE3 on cell proliferation (Figure S4E). These T-Rex cells expressed a single copy of the inserted transgene at a defined locus, which can be precisely induced to similar expression levels. Consistent with the data in UOK109 KO-rescue cell lines, under similar levels of transgene expression, SFPQ::TFE3 T-REx cells showed clear nuclear foci and high *GPNMB* expression, while SFPQΔCCD::TFE3 T-REx cells had fewer condensates and low *GPNMB* expression (Figures S4F-S4H). In accordance with the role of SFPQ::TFE3 condensates in promoting cancer, SFPQΔCCD::TFE3 T-REx cells that lack condensates proliferated slower (Figures S4I and S4J). Together, we found that the ability of TFE3 FO to form condensates contributed to cell proliferation and migration.

TFE3 FOs regulate CCD-dependent oncogenic transcriptional programs in tRCC

To elucidate the mechanisms by which TFE3 fusion-mediated condensate formation promotes cell proliferation, we investigated the impact of full-length TFE3 FOs and their ΔCCD counterparts on the transcriptome of tRCC cells. We performed RNA-seq in KO cells, and cell lines rescued with wild-type TFE3 (TFE3^{R}) or full-length TFE3 FOs (NONO::TFE3^{R}, SFPQ::TFE3^{R}) and their respective altered CCD mutants. Principal-component analysis (PCA) demonstrates that two TFE3 FOs form a distinct cluster separate from wild-type TFE3 (Figure 5A), depicting the unique transcriptomic changes induced by FOs. Interestingly, alterations in the CCD of TFE3 fusions also form a distinct cluster away from full-length FOs, highlighting their disruptive effect on global transcription (Figure

5A). Unsupervised hierarchical k-means clustering of all transcriptomes confirmed these observations (Figure S5A).

Analysis of differentially expressed genes revealed wide-spread changes in transcription with hundreds of genes being upregulated or downregulated in each condition (Figures 5B and S5B). We next applied k-means clustering to analyze differentially expressed genes between wild-type TFE3 and FOs, which revealed clear transcriptional differences between FOs and wild-type TFE3. Cluster 1 (C1) showed genes upregulated in the KO enrich for TNF signaling pathways using both gene ontology and gene set enrichment analyses (GSEA, Hallmark gene set) (Figures S5C and S5D). Cluster 2 (C2) exhibited genes that were downregulated in both fusions, while cluster 5 (C5) showed genes that were upregulated in both fusions and wild-type TFE3 (Figure 5C). Gene ontology for each cluster demonstrated that the most enriched gene pathways in FOs compared with TFE3 were related to the cell cycle (C2, C3, and C4) (Figure 5C), consistent with their effect on cell proliferation (Figures 4G, 4H, S4I, and 4J). Consistent with this, GSEA also showed that TFE3 FOs activate E2F, MYC targets, and the G2M checkpoint, which drive uncontrolled proliferation (Figures 5D and 5E). These results show that TFE3 FOs drive tRCC by activating a transcription program related to cell proliferation. Of note, all gained transcriptomic clusters in TFE3 FOs were enriched for canonical TFE3 target genes (Figure 5C), suggesting that the FOs may hijack the TFE3 transcriptional program. Deletion of, and mutation in, the CCD have similar effects (Figures S5E and 5F), which reversed the transcriptional programs of FOs (Figure 5F), underscoring the importance of condensate formation for gene expression by the FOs.

To quantify the impact of CCD alterations on FO-specific gene expression, we identified upregulated and downregulated genes in FOs compared with wild-type TFE3 and assessed how CCD alterations affected these genes. CCD alterations affected 44.4% of upregulated genes, 45.5% of downregulated genes (Figure S5F), and 44.9% (1,914 genes) of NONO::TFE3-specific genes (Figure 5G). For SFPQ::TFE3, CCD alterations impacted 46.2% of downregulated genes, 40.7% of upregulated genes (Figure S5E), and 43.4% (1,892 genes) overall (Figure 5G). These results (Figures 5G, S5F, and S5G) show that CCD alterations disrupt FO-dependent transcription. In CCD-altered samples, gene ontology revealed a loss of TFE3 targets and activation of TNF signaling and inflammation, suggesting that cells with CCD alterations reverted to transcriptional signatures similar to KO cells (Figure 5F). GSEA revealed that TFE3 FOs with defective CCD trigger a cytokine storm phenotype, similar to KO, with upregulation of TNF signaling, interferon response, and inflammatory pathways (Figure 5H),[37] validated by additional molecular signatures (Figure S5H). Leading edge analysis identified chemokines *CCL2*, *CXCL10*, and *CXCL11* as key genes driving TNF signaling (Figure 5I). Further analysis of the Cytokine Super-family[38] atlas showed that CCD perturbations activate a broad range of cytokines, particularly *IL1A* and *IL6*, which are linked to the cytokine storm phenotype[38] (Figure 5J). Altogether these findings highlight the CCD-dependent oncogenic gene expression driven by TFE3 FOs that fuel tRCC proliferation.

The CCDs of TFE3 FOs are critical for genome-wide reprogramming of canonical TFE3 cistrome

To understand if TFE3 FO condensates affect transcription directly through binding to new sites, we mapped the chromatin binding of TFE3 FOs using FLAG CUT&RUN. Consistent with RNA-seq, PCA of chromatin peaks revealed that TFE3 FOs exhibit a distinct profile compared with wild-type TFE3 (Figure 6A). CCD alterations in both FOs showed a similar chromatin binding pattern to each other but distinctly clustered away from their full-length FO counterparts (Figure 6A, inset). We then analyzed the overlapped chromatin binding peaks between different cell lines. NONO::TFE3 and SFPQ::TFE3 share most of their binding sites (Figure 6B), highlighting fusion partner-independent effects possibly due to condensate formation. Strikingly, around half of their binding sites are new compared with wild-type TFE3 binding sites (5,466 and 9,099 peaks for NONO::TFE3 and SFPQ::TFE3, respectively, Figure 6B), indicating that condensate formation may allow them to access new binding sites. To characterize these new binding sites, we performed k-means clustering of wild-type and TFE3 FOs and analyzed the TF motifs in each cluster by *de novo* HOMER motif analysis[39] (Figure 6C). We found that, while the TFE3 motif (CATGTG)[40] and AP-1 motif are shared among all three clusters, unique motifs also emerge in each cluster. MYC motif is present in C1 where wild-type TFE3 predominantly binds, whereas RUNX1 motif appears in C2 and C3, where NONO::TFE3 and SFPQ::TFE3 bind, respectively. These indicate that TFE3 FOs may cooperate with RUNX1 to drive the oncogenic program of tRCC. Mapping the chromatin binding sites based on their distance from transcription start sites (TSSs) revealed that TFE3 FOs preferentially target TSS-distal regulatory regions indicative of enhancers, whereas wild-type TFE3 is more frequently found at promoters (32% versus 9% for full-length FOs) (Figure 6C). Altogether these data indicate that TFE3 FOs, compared with the wild-type TFE3, bind to new sites on the genome.

We next examined differential binding sites associated with CCD alterations compared with full-length FOs. K-means clustering showed that CCD alterations caused significant changes in FO binding patterns, highlighting the role of condensate formation in TFE3 fusion binding (Figure 6D). CCD alterations impacted 1,560 upregulated peaks (21.3%), 956 downregulated peaks (12.4%) (Figure S6C), and 2,516 differential peaks in NONO::TFE3 regions (Figure 6E). Similar trends were observed in SFPQ::TFE3 (Figures 6E and S6D). TF motif analysis revealed that CCD alterations enriched MYC motifs instead of AP-1/RUNX1 motifs (Figure 6D), and decreased binding at TSS-distal regions (49% versus 97% for full-length FOs). These results suggest that CCD alterations revert TFE3 FO binding to wild-type TFE3.

Targeted treatments for tRCC are lacking since it is unknown what genes are specifically activated by TFE3 FOs compared with wild-type TFE3. Our RNA-seq and CUT&RUN data comparing wild-type TFE3, TFE3 FOs, and their respective CCD altered mutants in the same cell line background, provide a unique opportunity to identify these specific target genes. Integrating our RNA-seq and CUT&RUN data, we identified several known and novel TFE3 FO target genes, *GPNMB*[6,26,27], *NMRK2*,[28-30] *RTN4RL*, *EMILIN2*, *ULK4*, and *INPP5A* (Figures 6F and S6E) among others, where we also noted a significant reduction in binding in CCD alterations. A broad analysis integrating RNA-seq with FLAG

CUT&RUN revealed the top 50 NONO::TFE3- or SFPQ::TFE3-dependent upregulated and downregulated target genes, which also displayed the highest or lowest increase in chromatin binding profiles (Table S1).

Next, we sought to understand the mechanisms underpinning the altered binding of TFE3 FOs to their target genes. One possibility is that condensate formation creates a specialized environment around the target genes of TFE3 FOs, increasing the binding of TFE3 FOs to *cis*-regulatory elements and promoting transcription. To test this, we employed single-particle tracking (SPT) to measure the diffusion of TFE3, TFE3 FOs, and their CCD-altered forms. We used highly inclined and laminated optical microscopy to track individual molecules labeled with an organic dye, JFX554,[41] which covalently binds to the HaloTag on these molecules. We found that, while TFE3 FOs diffused slowly inside the nucleus, both wild-type TFE3 and CCD-altered TFE3 FOs diffused much faster (Figures 6G and 6H; Videos S8, S9, S10, S11, S12, and S13). In addition, the bound fraction of both TFE3 FOs is higher than wild-type TFE3 and their CCD-altered versions (Figure 6I). Taken together, these results suggest that the CCD, through the ability to form condensates, reduces the diffusion of TFE3 FOs and increases binding to their target genes to increase transcription in concert with other cofactors such as AP-1 and RUNX1.

TFE3 FO condensates remodel the chromatin landscape and enhancer activity in tRCC cells

To elucidate how TFE3 FOs condensates influence transcription at its target sites, we next assessed changes in chromatin accessibility by ATAC-seq (Figure S7A). Consistent with the transcriptomic and chromatin binding findings, k-means clustering of differential chromatin-accessible regions identified sites where accessibility is reduced by FOs compared with wild-type TFE3 in C2, as well as sites that have gained accessibility (C5), indicating the key role of FOs in altering the chromatin landscape of tRCC (Figure 7A). In both common accessible sites between the two FOs (C5), we observed TFE3 TF as the top motif, suggesting that the sites gaining accessibility in both FOs are TFE3-regulated loci. Consistent with the CUT&RUN data, the AP-1 motif was also enriched in these sites. In addition, we noted that, similar to our transcriptomic data (Figure 5), chromatin regions containing NF-κB-p65 were closed upon TFE3 FO rescue, leading to transcriptional repression of TNF signaling.

Our data also showed that most of these chromatin accessibility changes are at sites distal to TSSs (Figure 7A), indicative of enhancers, consistent with FLAG CUT&RUN data (Figure 6C) and IF data co-staining TFE3 FOs and H3K27ac (Figures 2A and 2B). To further validate this, we performed CUT&RUN of H3K27ac, which showed that sites gaining H3K27ac upon FO expression were enriched for AP-1 and TFE3 TFs (Figure S7B), aligning with the hypothesis that TFE3 FOs enhance chromatin accessibility at regulatory regions. Integration of ATAC-seq, FLAG CUT&RUN, and H3K27ac data revealed a strong correlation between TFE3 FO binding and enhancer formation, with C5 showing increased accessibility, enhanced TFE3 binding, and higher H3K27ac levels compared with wild-type and KO cells (Figure 7B). Together, these findings suggest that TFE3 FOs contribute to a unique chromatin landscape, promoting enhancer activation and transcriptional regulation.

To investigate how condensate formation influences TFE3 FO function, we examined how CCD alterations affect chromatin accessibility and enhancer dynamics. Altering CCD of TFE3 FOs led to a substantial closure of chromatin accessibility sites, suggesting that condensate formation is crucial for TFE3 FO-mediated chromatin remodeling (Figures 7C and S7C). Of note, the NONOmut::TFE3 fusion exhibited an intermediate phenotype, as reflected in PCA and cluster analysis (Figures 7C, S7A, and S7C). Overexpression of CCD-altered TFE3 fusions also led to increased accessibility at a significant number of sites (Figure 7C, $n = 813$, C4) that were enriched for AP-1 and NF-κB-p65 motifs, mimicking patterns observed in TFE3 KO cells (Figure 7A, C1). A separate analysis of H3K27ac binding peaks confirmed that CCD alterations also disrupted H3K27ac deposition, particularly at AP-1 and TFE3 sites, with regions showing increased acetylation enriched for the p65 motif (Figure S7D).

Integrating ATAC-seq, FLAG CUT&RUN, and H3K27ac data demonstrated that CCD alterations impaired TFE3 FO binding at target sites, resulting in decreased H3K27ac levels and reduced chromatin accessibility in C1, C2, and C3 (Figure 7D). In C4, where chromatin accessibility increased upon CCD alterations, H3K27ac levels were elevated, but TFE3 binding was only modestly increased, suggesting that derepression of TNF signaling in this cluster may involve TFE3 cooperation with other transcription factors such as p65. Approximately 40% of TFE3 FO binding sites overlapped with H3K27ac peaks, indicating potential cooperation with other TFs such as AP-1 to orchestrate their oncogenic program in tRCC cells (Figure S7E). Examples of gene tracks displaying integrated ATAC-seq, CUT&RUN FLAG, H3K27ac, and RNA-seq for target genes such as *GPNMB* and *ATG16L1* are shown in Figure 7E. In addition, the top 50 NONO::TFE3- or SFPQ::TFE3-dependent target genes—upregulated and downregulated genes—that also displayed the highest or lowest chromatin accessibility profile are shown in Table S2. Finally, quantification of differential chromatin accessibility and H3K27ac occupancy in NONO::TFE3 and SFPQ::TFE3 demonstrated that CCD alterations significantly reshape the chromatin landscape impacting 60%–90% of FO-specific chromatin accessibility (Figures S8A and S8B) and 14%–25% of H3K27ac deposition (Figures S8C and S8D). These results highlight that condensate formation is crucial for maintaining chromatin accessibility and enhancer regulation, likely by recruiting chromatin-modifying complexes.

Given that biomolecular condensates may drive super-enhancers (SEs),[42-44] we employed ROSE pipeline[45] to identify SEs from our H3K27ac CUT&RUN data (Figure S8E) and found 74 common SE-associated genes, including housekeeping genes such as *LIF* and *SMAD3* across all conditions and condition-specific SE activities (Figure 7F). Notably, tRCC driven by TFE3 FOs showed a significant increase in non-housekeeping SEs ($n = 111$), compared with wild-type TFE3 ($n = 9$) and other conditions (Figure 7F). These SEs included key survival and anti-apoptotic genes such as *BCL2* and a cancer stemness marker such as *CD44*,[46] with also increased TFE3 FO chromatin binding on these genes (Figure 7G). In contrast, CCD alterations did not activate these SEs but induced SE-associated genes such as *DDIT4* and *SERPINE1* involved in stress response and senescence[47,48] (Figure 7F). These results suggest that condensates reshape the chromatin landscape and promote oncogenesis in tRCC by regulating transcription at SEs.

DISCUSSION

Our results show that condensate formation is an essential feature of TFE3 FOs in tRCC. Using NONO::TFE3 and SFPQ::TFE3 as examples, we found that TFE3 FO condensates are associated with active transcription and increase cancer cell proliferation and migration. We have also undertaken a comprehensive genome-wide analysis of WT TFE3, TFE3 FOs, and their condensate-deficient mutants, showing that TFE3 FO condensates drive pro-oncogenic phenotypes by altering genomic binding, chromatin accessibility, and gene expression. This study improves our understanding of TFE3 FO-driven tRCC mechanisms, revealing new pathways and binding partners of TFE3 FOs, and highlighting potential therapeutic targets.

FOs are often primary driver mutations in specific cancers, yet their precise role in oncogenesis is unclear. Studies suggest that FOs bind to new genomic sites, altering genome organization. For example, in Ewing sarcoma, the EWS-FLI FO recruits the SWI/SNF complex to bind to new genomic sites (GGAA repeats), activating previously inaccessible target genes via condensate formation.[49-52] Similarly, NUP98 FOs form condensates that reorganize genome architecture for leukemia-specific gene expression,[13,14] with mutations in the FG repeats disrupting condensate formation and restoring genome architecture.[13] In our work, we identified that NONO:: and SFPQ::TFE3 FOs uniquely remodel the chromatin landscape, a characteristic typically associated with pioneer TFs. Sites accessible and bound by TFE3 FOs also exhibited binding by other TFs such as the AP-1 complex, suggesting potential cooperation between TFE3 and AP-1 in chromatin remodeling. Future investigations should explore the biochemical interactions between AP-1, TFE3 FOs, and possibly other TF partners that mediate TFE3 FO-driven oncogenesis. Moreover, while TFE3 FOs can bind to genomic sites overlapping with that of TFE3, they can also bind to new sites previously inaccessible to TFE3. We surmise that, since TFE3 FO condensates can increase dwell time on the DNA as shown in our SPT experiments, they may recruit diverse chromatin remodelers such as SWI/SNF or p300 to finely tune H3K27ac dynamics and alter chromatin accessibility, thereby fueling oncogenic transcriptional output and tumorigenesis in tRCC. The disruption of condensate formation, stemming from CCD alterations in FOs likely disrupts these processes. Further investigations are warranted to rigorously test these hypotheses, which may be a general mechanism by which condensate-forming FOs drive cancer progression.

While intrinsically disordered regions are the domains mainly considered to drive condensate formation, NONO::TFE3 and SFPQ::TFE3 condensates are formed via highly structured CCDs. CCDs represent one of the smallest well-understood protein-protein interaction motifs.[53] It is known that CCDs mediate homo- or hetero-dimerization and oligomerization among DBHS family proteins such as NONO and SFPQ.[17] This “emergent multi-valency”[54] likely drives the condensate formation of both NONO/SFPQ and NONO::TFE3/SFPQ::TFE3 fusions. Indeed, synthetic biology experiments have shown that the number of and specific residues of CCDs can be tuned to modulate condensate formation.[53] We also showed that mutating the a and d residues on the heptad repeats (CCDmut), which disrupts hydrophobic CCD interactions similar to CCD deletions, decreases condensate formation, chromatin accessibility, genome-wide TFE3 FO binding,

and SE formations. This underscores the crucial role of CCDs and condensate formation in shaping the chromatin landscape. These results also indicate that modulating CCD interactions can be an effective way to disrupt TFE3 FOs and treat tRCCs. CCDs are also common among other FOs such as BCR-ABL,[55] CBFβ-SMMHC,[56] and PCM1-JAK2,[57] implicated in the functions of these FOs. It remains to be determined whether CCDs in these FOs can drive condensate formation, and if targeting CCD interactions can be a general applicable way to target FOs.

Limitations of the study

Although we showed that CCDs drive TFE3 FO condensate formation and transcription activities, and they may do so by mediating interactions with other DBHS family members, the precise mechanisms of how CCDs mediate condensate formation are unclear. We also did not focus on studying RRMs, which have confounding effects on condensate formation and transcription. We constructed the SFPQ::TFE3^{R} and SFPQΔCCD::TFE3^{R} in UOK109 KO as we could not KO SFPQ::TFE3 in UOK145 cells. Further studies on SFPQ::TFE3 may benefit from KO SFPQ::TFE3 in additional SFPQ::TFE3 patient-derived cell lines.

STAR★METHODS

EXPERIMENTAL MODEL AND STUDY PARTICIPANT DETAILS

Cell lines and cell culture: All cell lines used were regularly tested for mycoplasma contamination (Mycoalert detection kit, LT07-318, Lonza) and were tested negative. Specific methods of authentication are detailed below.

HK-2, UOK109, and UOK145 cells: HK2 cells were from ATCC (CRL-2190). UOK109 and UOK145 cells were previously generated and generously provided by the Linehan Lab.[18,19] HK-2, UOK109, and UOK145 cells were grown in Dulbecco's Modified Eagle's Medium (DMEM, 15-013-CV, Corning) supplemented with 10% v/v fetal bovine serum (FBS, 26140079, Gibco), 1% v/v Penicillin-Streptomycin (10,000 U/mL) (15140122, Thermo Fisher), 1% v/v GlutaMAX Supplement (35050061, Thermo Fisher), and 1% v/v Mem Non Essential Amino Acids Solution (100X) (11140050, Thermo Fisher). Cells were grown at 37°C with 5% CO_2 in a humidified incubator. HK-2 cells were authenticated by STR profiling. UOK109 and UOK145 were authenticated using immunoblotting, confirming their expression of NONO::TFE3 and SFPQ::TFE3, respectively.

HEK293T and U-2 OS cells: HEK293T (CRL-3216) and U-2 OS (HTB-96) cells were from ATCC and were grown in DMEM supplemented with 10% v/v FBS, 1% v/v Penicillin-Streptomycin (10,000 U/mL), and 1% v/v GlutaMAX Supplement (35050061, Thermo Fisher) at 37°C with 5% CO_2 in a humidified incubator. HEK293T and U-2 OS cells were authenticated by STR profiling.

ACHN cells: ACHN cells were from ATCC (CRL-1611) and were grown in EMEM with L-Glutamine (112-018-101, Quality Biological) supplemented with 10% v/v FBS, 1% v/v Mem Non Essential Amino Acids Solution (100X), and 1% v/v sodium pyruvate (100 mM)

(11360070, Thermo Fisher) at 37°C with 5% CO_2 in a humidified incubator. ACHN cells were authenticated by STR profiling.

FU-UR-1 and FU-UR-2 cells: FU-UR-1 and FU-UR-2 cells were generously provided by Dr. Masako Ishiguro[58,59] and were grown in DMEM/F12 50:50 Mix (15-090-CV, Corning) supplemented with 10% v/v FBS, 1% v/v GlutaMAX Supplement at 37°C with 5% CO_2 in a humidified incubator. FU-UR-1 and FU-UR-2 cells were from Dr. Masako Ishiguro[58,59] and were not further authenticated.

Flp-In T-REx 293 cells: Flp-In T-REx 293 cells expressing Tet repressor were generously gifted by Dr. Philipp Oberdoeffer[60] and were grown in DMEM supplemented with 10% v/v FBS, Tet system approved, USDA-approved regions (A4736401, Gibco), 1% v/v Penicillin-Streptomycin (10,000 U/mL), 1% v/v GlutaMAX Supplement at 37°C with 5% CO_2 in a humidified incubator. Each cell line inducibly expressing TFE3:eGFP, SFPQ::TFE3:eGFP, SFPQΔCCD::TFE3:eGFP, NONO::TFE3:eGFP, and NONOΔCCD::TFE3:eGFP were created by co-transfecting the Flp-In T-REx 293 cells with pOG44 plasmid containing the flp recombinase construct and appropriate expression plasmids containing FRT sequences flanking the constructs of interest using Lipofectamine 3000 Transfection Reagent (L3000015, ThermoFisher). All expression constructs were made with the pcDNA5TM/FRT/TO-Flag vector (a gift from Dr. Michael Matunis) and the following primers for cloning our fusion:TFE3:eGFP constructs into the expression plasmids: NONO N terminus f: gactctagcgtttaaacttaatgcagagtaataaaacttttaacttgg; SFPQ N terminus f: gactctagcgtttaaacttaatgtctcgggatcggttc; TFE3 N terminus f: gactctagcgtttaaacttaatgtctcatgcggccgaac; eGFP C terminus r: tcagcgggtttaaacgggccggactcctcttccatgctg. Fusion TFE3 sequences were PCRed from custom Genscript plasmids also used in U-2 OS transfections. Plasmids were validated either by Sanger sequencing of the open reading frame or by whole-plasmid sequencing (Plasmidsaurus). For all experiments conducted with Flp-In T-REx 293 cells, the cells were plated in a 6-well plate, induced with 1 μg/mL doxycycline hyclate (D9891-1G, Sigma-Aldrich) in the medium the next day for 48 h, and then plated for each experiment. Flp-In T-REx 293 cells were not further authenticated.

UOK109 NONO::TFE3:eGFP KI cell line generation: C-terminally endogenously tagged UOK109 NONO::TFE3:eGFP KI cells were engineered using the CRISPR-Cas9 system. pTFE3-donor (Addgene #112377) and pTFE3.1.0-gDNA (Addgene #112473) were gifts from Dr. Kevin White. UOK109 cells were transfected with ATCC TransfeX (ACS-4005, ATCC) following the manufacturer's protocol. The cells were selected with 800 μg/mL G418 sulfate (30-234-CR, Corning) for 6 weeks and sorted into single colonies by fluorescence-activated cell sorting (FACS) and expanded. We extracted the genomic DNA from the selected clone using GeneJET Genomic DNA Purification Kit (K0721, Thermo Scientific) and performed PCR using the forward primer tcagtgtcccctgctgtctccaag and the reverse primer tctcatgtccttctccagccttct with Q5 High-Fidelity 2X Master Mix (M0492, NEB). The PCR product was gel extracted using Monarch DNA Gel Extraction Kit (T1020S, NEB) and verified using Sanger sequencing. We further validated the clone using imaging and immunoblotting (Figures S1D and S1E).

Frozen tRCC patient tissue samples: tRCC is a rare subtype of kidney cancer therefore, we were only able to obtain three de-identified frozen tRCC patient tissue samples from repositories, and we did not pre-determine the sample size. From the frozen tissue repositories, we selected patients diagnosed with tRCC. SFPQ::TFE3 patient 1 and PRCC::TFE3 patient 1 were seen at the Urologic Oncology Branch of the National Cancer Institute (NCI), National Institutes of Health (NIH) for clinical assessment (protocol NCI-89-C-0086 or NCI-97-C-0147). Known patient characteristics were as previously described.[6] SFPQ::TFE3 patient 2 was obtained from the Johns Hopkins Hospital Repository (IRB number: MOD00005088). The patient was diagnosed with SFPQ::TFE3 tRCC, other patient characteristics were not disclosed to the authors.

Mouse xenograft tumor of UOK109: Mouse xenograft tumors of UOK109 were created using 6–8 week-old NOD scid gamma (NSG mice) (Animal Research Service, Johns Hopkins University) in an Association for the Assessment and Accreditation of Laboratory Animal Care-accredited facility (protocol number MO20H243). UOK109 (5×10^6) cells were resuspended in Roswell Park Memorial Institute (RPMI) 1640 (Corning, 10-040-CM): Matrigel (354234, Corning) (1:1) and injected subcutaneously into the NSG mice. Mice were culled at 6–8 weeks post-injection and the tumors were harvested.

METHOD DETAILS

Immunoblot: Unless specified, cells were lysed using protein lysis buffer containing 50 mM Tris pH 8 (T60050–1000.0, Research Products International), 100 mM NaCl (S23025–3000.0, Research Products International), 1% Igepal CA-630 (56741-50ML-F, Sigma Aldrich), 0.5% Sodium deoxycholate (30970-25G, Sigma Aldrich), and cOmplete Mini Protease Inhibitor Cocktail (11836170001, Sigma Aldrich). UOK109 NONO::TFE3:eGFP KI and Flp-In T-REx 293 cells were lysed in 1x loading buffer containing 10% v/v glycerol (G5516, Sigma-Aldrich), 2% w/v sodium dodecyl sulfate (SDS, L3771, Sigma-Aldrich), 50 mM Tris pH 6.4, 1% 2-mercaptoethanol (M3148-25ML, Sigma-Aldrich) and 0.06% w/v bromophenol blue (1610404, Bio-Rad). Gel electrophoresis was performed using 4–12% Surepage Bis-Tris gel (M00654, GenScript) and transferred to Odyssey Nitrocellulose Membrane, 0.22 μm (926–31090, LI-COR Biosciences) at 100V for 60 min. The membrane was blocked for 1 h in 5% w/v skim milk powder in 1x TBS (351–086-101CS, Quality Biological) before treating with primary antibodies overnight at 4°C. Membrane was then treated with secondary antibodies for 1 h at room temperature before being imaged using Odyssey M (LI-COR Biosciences). Primary and secondary antibodies were diluted in 1x TBS containing 0.2% v/v Tween 20 (P7949-500ML, Sigma Aldrich). The antibodies used were anti-TFE3 antibody (HPA023881, lot number 18061, Millipore Sigma or AB93808, lot number GR3351483-14, Abcam; dilution 1:5000), anti-FLAG M2 antibodies (F3165-.2MG, Millipore Sigma, dilution 1:10 000), anti-GFP (MA5-15256, Invitrogen, dilution 1:5000), anti-β-actin antibodies (A9718, lot number 026M4757V, Millipore Sigma, dilution 1:10 000), IRdye 800CW goat-anti-rabbit (926–32211, lot number D10512-05, LI-COR Biosciences, dilution 1:20 000), IRdye 800CW donkey-anti-mouse (926–32212, lot number D10414-15, LI-COR Biosciences, dilution 1:20 000), and IRdye 680RD goat anti-mouse (926–68070, lot number D10512-15, LI-COR Biosciences, dilution 1:20 000).

Confocal microscopy: Unless indicated, confocal microscopy was performed on Zeiss LSM 900 with Airyscan 2 detector, Definite Focus 2, and temperature-controlled sample chamber with a CO_2 pump (for live cell imaging) with Plan-Apochromat 63x/1.40 Oil DIC f/ELYRA. The hardware was controlled with the Zeiss Zen software.

Immunofluorescence: Cells were seeded on circular cover glasses (72231-01, Electron Microscopy Sciences) in 24-well plates. After 24 h, cells were fixed with 4% w/v formaldehyde (12606S, Cell Signaling Technology) in 1x PBS for 10 min, permeabilized with 0.1% v/v Triton X-100 (T8787, Millipore Sigma) in 1x PBS for 15 min, and blocked in 3% w/v bovine serum albumin (BSA, A3294, Millipore Sigma) in 1x PBS for 30 min. Between every step, the cells were rinsed with 1x PBS. After blocking, the cells were incubated with primary antibodies diluted in 1% w/v BSA in 1x PBS overnight at 4°C. The following primary antibodies were used: anti-TFE3 antibody (1:1000; Thermo fisher, HPA023881), anti-RNA Pol II Ser5 antibody (1:1000; Abcam, ab5408), anti-RNA Pol II Ser2P (1:1000, Active Motif, 61083), anti-BRD4 antibody (1:2000; Cell Signaling, E4X7E), anti-H3K27ac antibody (1:1000; Active Motif, 39685), anti-H3K9me3 antibody (1:1000; Active Motif, 39285). After 3 washes with 1x PBS (10 min each), the cells were then incubated with secondary antibodies diluted in 1% w/v BSA in 1x PBS for 1 h in the dark at room temperature. The following secondary antibodies were used: Goat anti-Mouse IgG (H + L) Cross-Adsorbed Secondary Antibody, Alexa Fluor 568 (1:1000; Thermo fisher, A11031); Goat anti-Mouse IgG (H + L) Cross-Adsorbed Secondary Antibody, Alexa Fluor 647 (1:1000; Thermo fisher, A21235); Goat anti-Rabbit IgG (H + L) Cross-Adsorbed Secondary Antibody, Alexa Fluor 488 (1:1000; Thermo fisher, A11034); Goat anti-Rat IgG (H + L) Cross-Adsorbed Secondary Antibody, Alexa Fluor 647 (1:1000; Thermo fisher, A21247). After three washes (10 min each), the cell nuclei were stained with 0.1 μM Hoechst 33342 (62249, Thermo Scientific), washed once with 1x PBS (10 min), and mounted onto glass slides with Vectashield antifade mounting medium (H-1000-10, Vector Laboratories).

Tissue IF: Frozen patient samples (Figure 1F) were collected as described.[6] Deidentified frozen tRCC patient tissue (Figure S1B) was obtained from the Johns Hopkins Hospital Repository (IRB number: MOD00005088). Frozen patient samples and freshly harvested mouse xenograft tumors were fixed in 10% neutral buffered formalin (PFNBF-60, Azer Scientific) overnight, washed once with 1x PBS (30 min), incubated in 20% w/v sucrose (S5016-500G, Millipore Sigma) in 1x PBS for 24 h and then in 30% w/v sucrose in 1x PBS for 24 h. Tissues were then embedded in O.C.T. (4583, Sakura Finetek USA) at −80°C and cryosectioned at 10 μm onto a charged microscope slide (1255015, Fisher Scientific). Slides with mounted frozen tissue sections were dried for 1 h at 37°C and washed three times with 1x TBS containing 0.2% v/v Tween 20. We use a cryogenic marker (SM-1, SCIENCE-Marker) or a barrier seal (FNK-R-CSC096-01, DiagnoCINE) to create a hydrophobic barrier around the tissue, before continuing with standard immunofluorescence protocol at the permeabilization step. Images were Airyscan processed with the Zeiss Zen software (AF488 3.5 and DAPI 7.5, 3D processing).

1,6-Hexanediol treatment and imaging: UOK109 NONO::TFE3:eGFP KI cells were plated on Lab-Tek chambered coverglass (155409, Thermo Fisher) to be 70% confluent the next day. Cell nuclei were stained with 0.2 μM Hoechst 33342 (62249, Thermo Scientific) for 30 min and washed with medium twice before the experiment. Fluorescent images of the cells were taken using the Zeiss LSM 900 microscope with a 20× objective. 4 positions were selected from each well from each condition for imaging before treatment. Then, images were taken before and after the addition of medium with either 1% DMSO or 1% 1,6-hexanediol (88571, Sigma-Aldrich) every 5 min for 1 h.

Fluorescence recovery after photo bleaching (FRAP): UOK109 NONO::TFE3:eGFP KI cells were generated as described above. To generate stable cell lines expressing wildtype or TFE3 fusion oncoproteins in HEK293T cells, the cells were transfected with ATCC TransfeX following the manufacturer's protocol with plasmids containing NONO::TFE3:eGFP and SFPQ::TFE3:eGFP (pcDNA3.1(+)-C-eGFP vector, Genscript). Transfected cells were sorted by FACS 2 weeks after transfection. Since GFP positive cell population decreased, after every 6 weeks of culture, cells were again sorted by FACS.

Cells were plated in Lab-Tek chambered coverglass and imaged using Zeiss LSM 900. A region of interest was first selected in a rectangular box of approximately 1 μm × 1 μm in size. Five iterations of bleaching were done with a 488 nm laser at 100% power. Five and forty rounds of imaging were performed before and after bleaching, respectively, until the fluorescence signal plateau, at an interval of 5 s. The data was collected using the FRAP module of the Zen software. To quantify the half-time of fluorescence recovery ($t_{1/2}$), GraphPad (Prism) was used to fit a nonlinear regression curve with an exponential one-phase association to the normalized dataset after photobleaching.

***RNA fluorescence* in situ *hybridization (FISH)*:** To prevent RNA degradation, all reagents used were RNAse-free. Cells were seeded on circular cover glasses in 24-well plates. After 24 h, cells were fixed with 3.7% w/v formaldehyde in 1x PBS, rinsed once with 1x PBS, and then incubated in cold 100% ethanol (DP2818, Fisher Scientific) at 4°C overnight. We then followed the protocol for simultaneous IF + FISH in Adherent Cells from Stellaris RNA FISH Biosearch Technologies. The following RNA FISH Probes were used: Human NEAT1 with Quasar 570 Dye (ISMF-2037-1, Biosearch Technologies), Human ACTB intron for iceFISH with Quasar 570 Dye (ISMF-2002-5m Biosearch Technologies), Custom Human GPNMB intron with Quasar 670 Dye (custom against intron 1, Biosearch Technologies).

Transfection of U-2 OS cells: Unless otherwise indicated, full-length and domain deletion mutants of NONO::TFE3 and SFPQ::TFE3 were from Genscript, on a pcDNA3.1(+)-C-eGFP vector. pEGFP-N1-TFE3 was a gift from Shawn Ferguson (Addgene #38120). Unless otherwise indicated, we used Q5 to perform PCR and HiFi DNA Assembly (E2621X, NEB) to assemble the other custom constructs, according to the manufacturer's instructions. Plasmids were validated either by Sanger sequencing of the open reading frame or by whole-plasmid sequencing (Plasmidsaurus). To obtain (NONO)CCD::TFE3:eGFP, we PCR-ed using a plasmid containing NONO::TFE3 with primers f: tatagggagacccaagctggctagccatgTTTCCTCGTCCTGTGACTG, r: agtggatccgagctcggtaccGGACTCCTCTTCCATGCTG. To obtain NONO::TDP-43:TFE3,

we PCR-ed TDP-$43_{274-414}$ from cDNA created from UOK109 RNA lysate with primers f: tggaaggcactcattGGAAGATTTGGTGGTAATCCAG, r: cacaggcagcgcatcCATTCCCCAGCCAGAAGAC. To obtain FUS::TFE3:eGFP, we PCR-ed FUS_{1-267} using plasmids containing FUS.[88]

U-2 OS cells were seeded in 6-well plates with or without circular cover glasses and transfected the next day at ~70% confluency using Lipofectamine 3000 Transfection Reagent (L3000015, ThermoFisher). All transfections were performed at scaled-down (24-well plate) concentrations following the manufacturer's guidelines. After 48 h, the cells were either collected for RNA isolation or processed for imaging. For imaging, the cell coverslips were collected, fixed with 4% w/v PFA, rinsed with 1x PBS, and then incubated with Hoescht 33342 at RT for 10 min. After washing with 1x PBS for 10 min, 2 times, the coverslips were mounted on slides with Vectashield and sealed with nail polish.

Live cell imaging: Cells were plated on 8-chambered cover glass (C8-1-N, Cellvis) and changed to imaging media before imaging. The imaging media was FluoroBrite DMEM (A1896701, Gibco) supplemented with 10% v/v FBS, 1% v/v Penicillin-Streptomycin (10,000 U/mL), 1% v/v GlutaMAX Supplement, and 1% v/v Mem Non Essential Amino Acids Solution (100X). To image KO-rescue cells with HaloTag, cells were stained for 30 min with JF549-HaloTag ligand or JFX554-HaloTag ligand (100 nM, Janelia Materials).[41] Images were Airyscan processed with the Zeiss Zen software (AF568 3.5 and AF405 3.5, 2D processing).

Image analysis: Colocalization analysis - For 2D Pearson's correlation colocalization analysis of different channels, the "Coloc2" plugin in FIJI 67 was downloaded from https://github.com/fiji/Colocalisation_Analysis and utilized. Briefly, 2D images of cells at their center where the nuclear width is widest was taken using a 63x objective. The region of interest (ROI) of each cell nucleus was selected by thresholding the 405 nm Hoechst stain channel. The 2D ROI (nucleus) was used for colocalization analysis between two channels using the "Coloc2" plugin.

RNA fluorescence in situ hybridization (FISH) enrichment analysis - To evaluate the enrichment of immunofluorescence signal of TFE3 or fusion TFE3 at intron RNA FISH foci, we used a square region of interest (ROI) box centered around over 100 individual intron RNA FISH foci (GPNMB or ACTB) in 2D images using Fiji and duplicated both channels of interest. The duplicated ROI were combined into stacks for each channel and averaged using the "Z-project -> Average" function in Fiji. Then, we plotted the signal profile of a line drawn through the middle of each averaged image to determine enrichment.

Foci count analysis - For 2D analysis of foci count and analysis of relative fraction of fluorescence intensity in transfected U-2 OS cells, a custom-written FIJI script was used. Briefly, 2D images of cells at their center where the nuclear width is widest was taken using a 63x objective. A 2D region of interest (ROI) of each cell nucleus was selected by thresholding the 405 nm Hoechst channel. The mean intensity of the 488 nm channel (transfected construct) of each 2D ROI was measured. In each ROI, the number of foci was quantified by using the FIJI "find maxima" function with a prominence indicated in

the figure legends. To measure the fraction of fluorescence inside the foci in each ROI, the foci were selected by thresholding (1000, 65535) and the intensity and area of the foci were measured. Then, the area and mean intensity of the foci for each cell were multiplied and divided by the area multiplied by the mean intensity for the cell nucleus ROI to calculate the fraction of fluorescence inside the foci.

2D analysis of the foci count of UOK109 KO and rescue cells was performed with the custom-written FIJI script described above using a prominence value of 500. 2D images taken with a 63x object at live cell conditions were used for quantification.

Optogenetics: The template pHR-mCh-Cry2WT was a gift from Dr. Clifford Brangwynne (Addgene plasmid #101221). We modified the template between the MluI and NotI sites. Unless otherwise indicated, we used Q5 to perform PCR and HiFi DNA Assembly to assemble the other custom constructs, according to the manufacturer's instructions. Plasmids were validated either by Sanger sequencing of the open reading frame or by whole-plasmid sequencing (Plasmidsaurus). We modified pHR-mCh-Cry2WT slightly. We PCRed mCherry::Cry2WT using f: ggagctctcgagaattctcagccaccATGGTGTCTAAAGGCGAG, r: atgttgcaggtgggagttgcctacagcggccgctaTGCTGCTCCGATCATGATC. This allowed us to add a Kozak sequence gccacc before the mCherry sequence and remove the redundant 29 amino acids ARDPPVATGSGSGSGSGSAAATPTCNMRD at the C terminus of the open reading frame of the template.

To obtain other constructs with protein domains, we created another modified version of pHR-mCh-Cry2WT. We PCRed mCherry::Cry2WT using f: ggagctctcgagaattctcagcggccgcATGGTGTCTAAAGGCGAG, r: atgttgcaggtgggagttgctcatcaTGCTGCTCCGATCATGATC. This allowed us to add a NotI site before the mCherry sequence and remove the redundant 29 amino acids ARDPPVATGSGSGSGSGSAAATPTCNMRD at the C terminus of the open reading frame of the template. PCR products for different protein domains were inserted between the NotI site. We added a Kozak sequence gccacc and when required a start codon ATG before each protein domain.

HEK293T cells seeded in 8-chambered cover glass were transfected with 500 ng of plasmid in each well using Lipofectamine 3000 Transfection Reagent. After 48 h, the spent media was replaced with the FluoroBrite imaging media. We used the automated photo-manipulation module of the Zen software. First, we located multiple transfected cells and saved their locations. We selected cells that are far apart to minimize photoactivating nearby cells. After two initial images, each saved location was photoactivated using a 488 nm laser (10%). We imaged at 15 s intervals for 10 min.

To analyze the data, we used a custom-written FIJI script. ROIs were selected by thresholding the AF568 (mCherry) channel. In each ROI, the number of foci was quantified by using the FIJI "find maxima" function with a prominence of 700. As we found that the mCherry tag clustered into optoDroplet in photoactivated cells and we could no longer see clear cell boundaries, we could not reliably segment every single cell after

photomanipulation. Therefore, we measured all the mCherry positive ROIs in each image and normalized foci count by pixels.

EdU cell proliferation assay: Cells were plated in 8-chambered cover glass (C8-1-N, Cellvis) to be 70% confluent the next day. Then the Click-iT EdU Proliferation assay kit (C11008, Thermo Fisher Scientific) was used following the manufacturer's protocol. Cells were treated with EdU for 1 h. To quantify the number of proliferating cells, an in-house pipeline was used in CellProfiler[65] to obtain nuclei count and intensity of EdU signal in each nucleus for each image. Then, an intensity cutoff was set for each dataset and used to determine the number of nuclei with and without EdU signal.

Coimmunoprecipitation assay: Cells were collected and lysed using protein lysis buffer. For each sample, 50 μL of pierce Anti-DYKDDDDK Magnetic Agarose (A36797, Thermo Scientific) was used. Magnetic racks were used for all collection and washing steps. Beads were washed once in protein lysis buffer and twice in PBS with 0.02% v/v Tween (PBST). 200 μg of protein was added and brought up to a volume of 600 μL with PBST. Samples were incubated overnight at 4°C on a rocking platform. Supernatant was collected and the beads were washed 3 times in PBST and moved to new vials for collection. Proteins were eluted from the beads using 0.1M glycine pH 2.8 and shaking at 14,000 rpm at room temperature for 5 min. The eluants were neutralized with 1M Tris pH 9 (J62085.K2, Thermo Scientific) using 15% of the eluants volume.

Single-particle tracking: Single-particle imaging was performed on a Nikon Ti2-E Motorized TIRF System equipped with an x100/NA 1.49 oil-immersion Apo TIRF objective, a Back-Thinned CMOS camera system (Hamamatsu ORCA Fusion BT), a perfect focus system to account for axial drift, and an incubation chamber maintaining a humidified 37 °C atm with 5% CO_2 (Tokai Hit). The hardware was controlled with the Nikon NIS-Elements software. Images were obtained at 16-bit (no binning), 10 ms exposure, 20% 561 nm laser (LUN-F XL), 512x512 pixels. The pixel size of the recorded images was 0.065 μm. Cells were stained for 30 min with a low concentration of JFX554-HaloTag ligand (2 nM, Janelia Materials) to achieve sparse labeling. Cells were then washed twice, 5 min between each wash. The imaging media was FluoroBrite DMEM supplemented with 10% v/v fetal bovine serum, 1% v/v Penicillin-Streptomycin (10,000 U/mL), 1% v/v GlutaMAX Supplement, and 1% v/v Mem Non Essential Amino Acids Solution (100X). Samples were equilibrated in the incubation chamber for at least 10 min and a 5% laser was used to locate single cells. We took an initial image that will be used for nuclear segmentation later. To collect the images for single-particle tracking, we used 20% laser, 10 ms exposure with fast scan mode. We waited until ~10–12 well-separated single particles were seen (~2–3 min) and collected 5000 frames of consecutive imaging (no wait time), 4 movies each cell (to limit each file size) with a 16-bit format, region of interest (ROI) 512x512 pixels. We performed three independent repeats (imaging) for each rescue cell and eight cells for each repeat.

As we were interested in the protein of interest in the nucleus, we segmented the nuclear region using FIJI using a semi-automated custom-written FIJI script. Briefly, we used the Trainable Weka Segmentation plugin to create a mask using the initial image. The mask was

manually inspected and adjusted if necessary. As the total imaging time was less than 5 min in total, we assumed minimal image drift during image collection. We used the same mask to segment out the nuclear region of the 4 movies and converted the segmented images into TIFF format.

To localize and track single particles, we used a MATLAB implementation (Slimfast.m) of the MTT algorithm[61] with the following settings: Localization error: $10^{-6.25}$; deflation loops: 0; Blinking (frames): 1; max D (μm^2/s): 10. Then, we used a MATLAB code (https://gitlab.com/tjian-darzacq-lab/write_4dn_spt_format_matlab) to read in and merge the localized and tracked results. We further processed the data using a custom-written R code. As we previously merged data from four movies, the “trajectory”, “time”, and “frame” parameters were not indexed uniquely (e.g., every movie has trajectory 1, time 0 s, and frame 1). Therefore, we re-indexed the “trajectory”, “time”, and “frame” such that these parameters were sequential and unique. To minimize tracking errors, we then filtered out frames with more than ten detections. During nuclear segmentation, sometimes, the edges were not smooth and were wrongly identified as a spot/detection. Since these artificial detections did not move, they appeared as artificial “trajectories” that were exceedingly long (i.e., they persisted across frames). We defined detections that persisted for more than 10% of imaging time (500 frames) as artifacts and we filtered these trajectories out. Finally, we saved the cleaned data as a CSV file.

We used saSPT (https://github.com/alecheckert/saspt)[62,89] to analyze the single-particle trajectories with the following settings: diff_coefs: np.logspace(−4.0, 1.5, 200), loc_errors: np.linspace(0.00, 0.07, 20), likelihood_type: RBME, pixel_size_um: 0.065, frame_interval: 0.01 s, and focal_depth: 0.7. We calculated the mean diffusion coefficients using the posterior occupation at each diffusion coefficient for each cell. We calculated the fraction of trajectories with diffusion coefficients <0.15 μm^2 by summing the posterior occupation with diffusion coefficients less than 0.15 μm^2.

Scratch wound healing assay: Widefield microscopy of scratch wound healing assay was performed on the Ti2-E epifluorescence module with a CFI60 Plan Apochromat Lambda D x10/NA 0.45 DIC objective, a Back-Thinned CMOS camera system (Hamamatsu ORCA Fusion BT), a perfect focus system to account for axial drift, and an incubation chamber maintaining a humidified 37 °C atm with 5% CO2 (Tokai Hit). The hardware was controlled with the Nikon NIS-Elements software. Images were obtained at 16-bit (no binning) and 9 ms frame rate. 1x10^5 Cells were seeded in 12-well plastic plates to be confluent on the day of the experiment. After 24 h, cells were treated with 0.625 μM aphidicolin to eliminate the confounding effects from cell proliferation. After 24 h (48 h after seeding), a 20 μL pipette tip was used to create one horizontal and one vertical line across the center of each well. The cells were washed twice with medium and replaced with fresh medium containing 0.625 μM aphidicolin. After the scratch was created, brightfield images were taken every 1 h for 24 h for 8 fields of view for each cell line. A total of 3 biological replicates were conducted. To quantify the area fraction of wound closed every hour, the FIJI plugin from https://github.com/AlejandraArnedo/Wound-healing-size-tool was downloaded and used. The area fraction of the wound was normalized to the starting area fraction of the wound.

Cell morphology: To image the morphology of cells in different rescue cell lines, cells were plated sparsely in 6×-well plates and brightfield images were taken using a light microscope with INFINITY camera and 10× objective. Then, CellPose[64] was used to create masks for each cell in the image. The masks were used in CellProfiler in an in-house pipeline to quantify cell morphology. The “eccentricity” measurement was used as a parameter for morphology. A cell with a value of 1 is in the shape of a line while a cell with a value of 0 is perfectly circular. The eccentricity of all the cells in an image was averaged to give a mean eccentricity value for each image.

RNA-seq: Cells were detached using accutase (A6964, Sigma-Aldrich), diluted in complete media and counted. One million cells were pelleted and the supernatant was aspirated. Cell pellets were snap frozen and stored in −80°C freezer until RNA isolation. Total RNA was extracted using RNeasy Mini Kit (74104, Qiagen) and RNase-Free DNase Set (79254, Qiagen) according to the manufacturer’s instructions. Human mRNA sequencing (polyA enriched) was performed at Novogene with NovaSeq PE150 (6 G raw data per sample). The RNA-seq data underwent initial processing with fastp[67,68] for quality trimming of fastq files. Subsequently, transcript quantification was performed using Salmon.[69] Differential gene expression analysis was performed using DESeq2[70] and the peaks were categorized into up-regulated (log2FC ≥ 0.5, padj <0.05) and down-regulated (log2FC ≤ −0.5, padj <0.05). The differential peaks between two groups of conditions were included and clustered using the k-means function in R after normalizing to Z score. Heatmaps were then generated using ComplexHeatmaps,[71,72] with the number of k-means clusters manually adjusted for biological relevance. Gene Set Enrichment Analysis (GSEA)[73,74] and Gene Set Variation Analysis (GSVA)[75] were conducted« against MSigDB pathways[76,77] using DESeq2-normalized data. Alignment to the hg38 reference genome was performed using STAR v2.7.8a,[78] and track plots were generated using bwtool and trackplot.[79,80]

ATAC-seq: ATAC-seq samples were prepared as previously described[90] using the Illumina Tagment DNA Enzyme and Buffer Kit (20034197, Illumina). We used 50,000 cells for each reaction. Upon transposition, we cleaned up the reaction using a Zymo DNA Clean and Concentrator-5 Kit (D4014, Zymo) according to the manufacturer’s protocol. We amplified the eluted DNA using 2x NEBNext Q5 Hotstart HiFi PCR Master Mix (M0543L, NEB) for 11 cycles. We purified the amplified libraries using the Zymo DNA Clean and Concentrator-5 Kit.

CUT&RUN-seq: We lightly fixed the cells with 0.4% w/v PFA for 1 min and quenched using 0.125 M glycine for 5 min. Cells were pelleted and washed once with PBS. Cell pellets were snap-frozen and stored in −80°C freezer until being processed. CUT&RUN were performed with Epicypher’s CUTANA CUT&RUN kit v3 and library preparation kit v1.1 following the manufacturer’s instructions using an FLAG antibody (CST 14793, Cell Signaling) and H3K27Ac antibody (39034, Active Motif). No E. coli spike-in was used. Library quality and concentrations were assessed using the D1000 TapeStation system (Agilent). Libraries were sequenced for 25 cycles in 75-bp paired-end mode on Illumina Novaseq 6000 and data were analyzed as described.

ATAC-seq and CUT&RUN-seq analyses: For both CUT&RUN and ATAC-seq analyses, initial steps involved trimming raw fastq files using fastp. Subsequently, reads were aligned to the hg38 genome assembly using bowtie2 v2.5.2.[81] Duplicate reads in ATAC-seq data were removed using PICARD's MarkDuplicates.[82] Peak calling was performed using MACS2,[83] followed by merging peaks into a comprehensive peak atlas. Peak intensities per sample were quantified from bam files, generating a peak-by-sample matrix. Differential analysis, heatmaps, and track plots were generated similarly to the RNA-seq workflow. Motif discovery and peak annotations per cluster in heatmaps were conducted using HOMER findMotifsGenome.pl and annotatePeaks.pl,[39] respectively. Overlapping peaks were identified using ChIPpeakAnno[84] to create Venn diagrams. Profile plots were generated using deepTools v.3.5.1.[85]

Super-enhancer analysis: Superenhancer-associated genes are generated based on the ROSE pipeline using H3K27ac CUT&RUN datasets with the default parameters.[45,86] For each condition, super-enhancers present in all three replicates are identified and filtered to keep super-enhancers that are found in at least two replicates. Overlap analysis is made using DeepVenn.[87]

qRT-PCR: Samples were collected and lysed using RNeasy Lysis Buffer (79216, Qiagen). RNA was isolated using the Direct-zol RNA MiniPrep Kits (R2052, Zymogen) according to the manufacturer's instructions. cDNA was generated using the High-Capacity RNA-to-cDNA Kit (4388950, Applied Biosystems) according to the manufacturer's protocol without RNase inhibitors. qPCR reactions were conducted using standard amplification cycle and melt curve analysis settings on the QuantStudio3 Real-Time PCR System using PowerUp SYBR Green Master Mix for qPCR (A25742, Applied Biosystems) according to the user guide. All target gene expressions were normalized to the expression of GAPDH in each cell line. The values were then normalized to the control for each experiment.

Vectors, lentivirus production, and infection to create the UOK109 KO-rescue model: CRISPR/Cas9 plasmids were constructed from pSpCas9(BB)-2A-GFP (PX458) (a gift from Dr. Feng Zhang Addgene plasmid #48138). Short guide sequence AGTTCGTTGGACACATACTG was cloned between the BbsI site as previously described.[91] UOK109 cells were transfected using Lipofectamine 3000 Transfection Reagent. Transfected cells were sorted for GFP-positive cells using FACS and expanded. We used limiting dilution to obtain clonal cells to select for KO cells. KO cells were validated as described in the validation of the UOK109 NONO::TFE3:eGFP KI cell line. The primers for PCR were, f: ccaggatgatctcgatctcctg and r: ctccaactcctgacctcagg.

Unless otherwise indicated, all lentiviral constructs were made with the pHIV-EGFP lentiviral vector (a gift from Drs. Bryan Welm and Zena Werb, Addgene plasmid #21373). We first made 3xFLAG::HaloTag:NONO::TFE3 using HiFi DNA Assembly between the NotI sites. 3xFLAG was PCR-ed from a gBlock (IDT) with primers (f: ttttcttccatttcaggtgtcgtgagctagccaccATGGACTACAAAGACCATG, r:catggaacctccCTTGTCATCGTCATCCTTG). Before 3xFLAG, we added an NheI site and a Kozak sequence. After 3xFLAG, we added a short linker GGS. HaloTag was PCR-ed from a plasmid containing HaloTag[92,93] with

primers (f: TGACGATGACAGGaGAGGtTCCATGGCAGAAATCGGTACTGGC, r: CACCAGCTGCAGATCCGGCGGAGCCAGGAGCGCCGCCGGAAATCTCGAGCGTC). After HaloTag, we added the linker sequence GAPGSAGSAAGGSG, to prevent HaloTag from interfering with the protein interactions and function.[94,95] NONO::TFE3 was PCR-ed from plasmid containing NONO::TFE3 (GeneScript) with primers (f: CCGGATCTGCAGCTGGTGGaTCcGGAatgcagagtaataaaactttaacttggag, r: cgatcgaggtcgacggtatcgatgcggccgctTCAGGACTCCTCTTCCATG). We then used the resulting 3xFLAG::HaloTag:NONO::TFE3 to create the other rescue constructs, between the BamHI and EcoRI sites. PCR products used to create 3xFLAG::HaloTag:NONOΔCCD::TFE3 and 3xFLAG::HaloTag:NONOmut:TFE3 used the primers f: CCGGATCTGCAGCTGGTGGaTCcGGAatgcagagtaataaaactttaacttggag, r: ctgcagttctagttcctgaattc with plasmids containing the gene-of-interest (GeneScript). PCR products used to create 3xFLAG::HaloTag:SFPQ::TFE3 and 3xFLAG::HaloTag:SFPQΔCCD::TFE3 used the primers f: CCGGATCTGCAGCTGGTGGaTCcGGAATGTCTCGGGATCGGTTC, r: ctgcagttctagttcctgaattc with plasmids containing the gene-of-interest (GeneScript). 3xFLAG::HaloTag:TFE3 used the primers f: cgccggatctgcagctggtggatccggaATGTCTCATGCGGCCGAACCAG, r: ctgcagttctagttcctgaattc with the plasmid containing the gene-of-interest (Addgene #38120).

Lentiviral particles were produced by transfection using Lipofectamine 2000 (Invitrogen) on HEK293T cells with third-generation packaging plasmids, pMDLg/pRRE, pRSV-Rev, and pMD2.G (gifts from Dr. Didier Trono Addgene plasmids #12251, #12253, and #12259). We changed the media 24 h after transfection and the medium containing viral particles was collected twice (48 and 72 h after transfection). Viral media was frozen at −70°C until transduction. KO cells were transduced with the viral media in the presence of polybrene (8 μg/mL), expanded, and sorted using FACS at least 48 h after viral infection. We stained cells with JF549-HaloTag ligand or JFX554-HaloTag ligand (100 nM) for 30 min and gated at similar intensities for various rescue cells to achieve comparable expression levels.

QUANTIFICATION AND STATISTICAL ANALYSIS

Unless indicated, GraphPad Prism Software was used for statistical analysis. GraphPad notation for p values was used on our reports: (ns = non-significant $p > 0.05$, *$p \leq 0.05$, **$p \leq 0.01$, ***$p \leq 0.001$, ****$p \leq 0.0001$). No randomization was performed. Unless indicated, no data was excluded from the analysis. All of the statistical details of experiments can be found in the figure legends.

Supplementary Material

Refer to Web version on PubMed Central for supplementary material.

ACKNOWLEDGMENTS

We thank Anthony Leung, Andrew Ewald, and members of the Cai and Toska Labs for feedback and discussions; Alec Heckert, Shasha Chong, Shawn Yoshida, and Xiaona Tang for advice on SPT experiments; Philipp Oberdoerffer for the Flp-In T-REx 293 cells; and Xiaoling Zhang at the JHU Ross Flow Cytometry Core for

technical assistance on FACS. This work is supported by the Jayne Koskinas Ted Giovanis Foundation for Health and Policy grant (to E.T.), and the Johns Hopkins Provost Catalyst Award (to E.T.).

REFERENCES

1. Kauffman EC, Ricketts CJ, Rais-Bahrami S, Yang Y, Merino MJ, Bottaro DP, Srinivasan R, and Linehan WM (2014). Molecular genetics and cellular features of TFE3 and TFEB fusion kidney cancers. Nat. Rev. Urol 11, 465–475. 10.1038/nrurol.2014.162. [PubMed: 25048860]
2. Geller JI, Ehrlich PF, Cost NG, Khanna G, Mullen EA, Gratias EJ, Naranjo A, Dome JS, and Perlman EJ (2015). Characterization of adolescent and pediatric renal cell carcinoma: A report from the Children's Oncology Group study AREN03B2. Cancer 121, 2457–2464. 10.1002/cncr.29368. [PubMed: 25845370]
3. Bakouny Z, Sadagopan A, Ravi P, Metaferia NY, Li J, AbuHammad S, Tang S, Denize T, Garner ER, Gao X, et al. (2022). Integrative clinical and molecular characterization of translocation renal cell carcinoma. Cell Rep. 38, 110190. 10.1016/j.celrep.2021.110190. [PubMed: 34986355]
4. Sidhar SK, Clark J, Gill S, Hamoudi R, Crew AJ, Gwilliam R, Ross M, Linehan WM, Birdsall S, Shipley J, and Cooper CS (1996). The t(X;1)(p11.2;q21.2) translocation in papillary renal cell carcinoma fuses a novel gene PRCC to the TFE3 transcription factor gene. Hum. Mol. Genet 5, 1333–1338. 10.1093/hmg/5.9.1333. [PubMed: 8872474]
5. Weterman MA, Wilbrink M, and Geurts van Kessel A. (1996). Fusion of the transcription factor TFE3 gene to a novel gene, PRCC, in t(X;1)(p11;q21)-positive papillary renal cell carcinomas. Proc. Natl. Acad. Sci. USA 93, 15294–15298. 10.1073/pnas.93.26.15294. [PubMed: 8986805]
6. Lang M, Schmidt LS, Wilson KM, Ricketts CJ, Sourbier C, Vocke CD, Wei D, Crooks DR, Yang Y, Gibbs BK, et al. (2023). High-throughput and targeted drug screens identify pharmacological candidates against MiT-translocation renal cell carcinoma. J. Exp. Clin. Cancer Res 42, 99. 10.1186/s13046-023-02667-4. [PubMed: 37095531]
7. Chen F, Zhang Y, Şenbabaoğlu Y, Ciriello G, Yang L, Reznik E, Shuch B, Micevic G, De Velasco G, Shinbrot E, et al. (2016). Multilevel Genomics-Based Taxonomy of Renal Cell Carcinoma. Cell Rep. 14, 2476–2489. 10.1016/j.celrep.2016.02.024. [PubMed: 26947078]
8. Sun G, Chen J, Liang J, Yin X, Zhang M, Yao J, He N, Armstrong CM, Zheng L, Zhang X, et al. (2021). Integrated exome and RNA sequencing of TFE3-translocation renal cell carcinoma. Nat. Commun 12, 5262. 10.1038/s41467-021-25618-z. [PubMed: 34489456]
9. Malouf GG, Monzon FA, Couturier J, Molinié V, Escudier B, Camparo P, Su X, Yao H, Tamboli P, Lopez-Terrada D, et al. (2013). Genomic heterogeneity of translocation renal cell carcinoma. Clin. Cancer Res 19, 4673–4684. 10.1158/1078-0432.Ccr-12-3825. [PubMed: 23817689]
10. Banani SF, Lee HO, Hyman AA, and Rosen MK (2017). Biomolecular condensates: organizers of cellular biochemistry. Nat. Rev. Mol. Cell Biol 18, 285–298. 10.1038/nrm.2017.7. [PubMed: 28225081]
11. Shin Y, and Brangwynne CP (2017). Liquid phase condensation in cell physiology and disease. Science 357, eaaf4382. 10.1126/science.aaf4382. [PubMed: 28935776]
12. Boulay G, Sandoval GJ, Riggi N, Iyer S, Buisson R, Naigles B, Awad ME, Rengarajan S, Volorio A, McBride MJ, et al. (2017). Cancer-Specific Retargeting of BAF Complexes by a Prion-like Domain. Cell 171, 163–178.e19. 10.1016/j.cell.2017.07.036. [PubMed: 28844694]
13. Ahn JH, Davis ES, Daugird TA, Zhao S, Quiroga IY, Uryu H, Li J, Storey AJ, Tsai YH, Keeley DP, et al. (2021). Phase separation drives aberrant chromatin looping and cancer development. Nature 595, 591–595. 10.1038/s41586-021-03662-5. [PubMed: 34163069]
14. Chandra B, Michmerhuizen NL, Shirnekhi HK, Tripathi S, Pioso BJ, Baggett DW, Mitrea DM, Iacobucci I, White MR, Chen J, et al. (2022). Phase Separation Mediates NUP98 Fusion Oncoprotein Leukemic Transformation. Cancer Discov. 12, 1152–1169. 10.1158/2159-8290.Cd-21-0674. [PubMed: 34903620]
15. Davis RB, Kaur T, Moosa MM, and Banerjee PR (2021). FUS onco-fusion protein condensates recruit mSWI/SNF chromatin remodeler via heterotypic interactions between prion-like domains. Protein Sci. 30, 1454–1466. 10.1002/pro.4127. [PubMed: 34018649]
16. Wang B, Gan W, Han X, Liu N, Ma T, and Li D. (2021). The positive regulation loop between NRF1 and NONO-TFE3 fusion promotes phase separation and aggregation of NONO-TFE3

in NONO-TFE3 tRCC. Int. J. Biol. Macromol 176, 437–447. 10.1016/j.ijbiomac.2021.02.061. [PubMed: 33592266]

17. Knott GJ, Bond CS, and Fox AH (2016). The DBHS proteins SFPQ, NONO and PSPC1: a multipurpose molecular scaffold. Nucleic Acids Res. 44, 3989–4004. 10.1093/nar/gkw271. [PubMed: 27084935]
18. Anglard P, Trahan E, Liu S, Latif F, Merino MJ, Lerman MI, Zbar B, and Linehan WM (1992). Molecular and cellular characterization of human renal cell carcinoma cell lines. Cancer Res. 52, 348–356. [PubMed: 1345811]
19. Clark J, Lu YJ, Sidhar SK, Parker C, Gill S, Smedley D, Hamoudi R, Linehan WM, Shipley J, and Cooper CS (1997). Fusion of splicing factor genes PSF and NonO (p54nrb) to the TFE3 gene in papillary renal cell carcinoma. Oncogene 15, 2233–2239. 10.1038/sj.onc.1201394. [PubMed: 9393982]
20. Baker BM, and Chen CS (2012). Deconstructing the third dimension: how 3D culture microenvironments alter cellular cues. J. Cell Sci 125, 3015–3024. 10.1242/jcs.079509. [PubMed: 22797912]
21. Kroschwald S, Maharana S, and Simon AW (2017). Hexanediol: a chemical probe to investigate the material properties of membrane-less compartments.
22. Nikolov DB, and Burley SK (1997). RNA polymerase II transcription initiation: a structural view. Proc. Natl. Acad. Sci. USA 94, 15–22. 10.1073/pnas.94.1.15. [PubMed: 8990153]
23. Shi J, and Vakoc CR (2014). The mechanisms behind the therapeutic activity of BET bromodomain inhibition. Mol. Cell 54, 728–736. 10.1016/j.molcel.2014.05.016. [PubMed: 24905006]
24. Creyghton MP, Cheng AW, Welstead GG, Kooistra T, Carey BW, Steine EJ, Hanna J, Lodato MA, Frampton GM, Sharp PA, et al. (2010). Histone H3K27ac separates active from poised enhancers and predicts developmental state. Proc. Natl. Acad. Sci. USA 107, 21931–21936. 10.1073/pnas.1016071107. [PubMed: 21106759]
25. Komarnitsky P, Cho EJ, and Buratowski S. (2000). Different phosphorylated forms of RNA polymerase II and associated mRNA processing factors during transcription. Genes Dev. 14, 2452–2460. 10.1101/gad.824700. [PubMed: 11018013]
26. Hong SB, Oh H, Valera VA, Baba M, Schmidt LS, and Linehan WM (2010). Inactivation of the FLCN tumor suppressor gene induces TFE3 transcriptional activity by increasing its nuclear localization. PLoS One 5, e15793. 10.1371/journal.pone.0015793. [PubMed: 21209915]
27. Baba M, Furuya M, Motoshima T, Lang M, Funasaki S, Ma W, Sun HW, Hasumi H, Huang Y, Kato I, et al. (2019). TFE3Xp11.2 Translocation Renal Cell Carcinoma Mouse Model Reveals Novel Therapeutic Targets and Identifies GPNMB as a Diagnostic Marker for Human Disease. Mol. Cancer Res 17, 1613–1626. 10.1158/1541-7786.Mcr-18-1235. [PubMed: 31043488]
28. Chen Y, Yang L, Lu Y, Liu N, Ma W, Fan H, Hu Q, Han X, Gan W, and Li D. (2022). Up-regulation of NMRK2 mediated by TFE3 fusions is the key for energy metabolism adaption of Xp11.2 translocation renal cell carcinoma. Cancer Lett. 538, 215689. 10.1016/j.canlet.2022.215689. [PubMed: 35447281]
29. Chen Y, Lu Y, Yang L, Ma W, Dong Y, Zhou S, Liu N, Gan W, and Li D. (2023). LncRNA like NMRK2 mRNA functions as a key molecular scaffold to enhance mitochondrial respiration of NONO-TFE3 rearranged renal cell carcinoma in an NAD(+) kinase-independent manner. J. Exp. Clin. Cancer Res 42, 252. 10.1186/s13046-023-02837-4. [PubMed: 37770905]
30. Feng H, Cao S, Fu S, Liu J, Gao Y, Dong Z, Cai T, Wen L, Xiong Z, Li S, et al. (2024). NMRK2 is an efficient diagnostic indicator for Xp11.2 translocation renal cell carcinoma. J. Pathol 264, 228–240. 10.1002/path.6340. [PubMed: 39092712]
31. Holehouse AS, Ginell GM, Griffith D, and Böke E. (2021). Clustering of Aromatic Residues in Prion-like Domains Can Tune the Formation, State, and Organization of Biomolecular Condensates. Biochemistry 60, 3566–3581. 10.1021/acs.biochem.1c00465. [PubMed: 34784177]
32. Davis RB, Supakar A, Ranganath AK, Moosa MM, and Banerjee PR (2024). Heterotypic interactions can drive selective co-condensation of prion-like low-complexity domains of FET proteins and mammalian SWI/SNF complex. Nat. Commun 15, 1168. 10.1038/s41467-024-44945-5. [PubMed: 38326345]

33. Lee M, Sadowska A, Bekere I, Ho D, Gully BS, Lu Y, Iyer KS, Tre-whella J, Fox AH, and Bond CS (2015). The structure of human SFPQ reveals a coiled-coil mediated polymer essential for functional aggregation in gene regulation. Nucleic Acids Res. 43, 3826–3840. 10.1093/nar/gkv156. [PubMed: 25765647]

34. Shin Y, Berry J, Pannucci N, Haataja MP, Toettcher JE, and Brangwynne CP (2017). Spatiotemporal Control of Intracellular Phase Transitions Using Light-Activated optoDroplets. Cell 168, 159–171.e14. 10.1016/j.cell.2016.11.054. [PubMed: 28041848]

35. Portz B, Lee BL, and Shorter J. (2021). FUS and TDP-43 Phases in Health and Disease. Trends Biochem. Sci 46, 550–563. 10.1016/j.tibs.2020.12.005. [PubMed: 33446423]

36. Boyd-Shiwarski CR, Shiwarski DJ, Griffiths SE, Beacham RT, Norrell L, Morrison DE, Wang J, Mann J, Tennant W, Anderson EN, et al. (2022). WNK kinases sense molecular crowding and rescue cell volume via phase separation. Cell 185, 4488–4506.e20. 10.1016/j.cell.2022.09.042. [PubMed: 36318922]

37. Tisoncik JR, Korth MJ, Simmons CP, Farrar J, Martin TR, and Ka-tze MG (2012). Into the eye of the cytokine storm. Microbiol. Mol. Biol. Rev 76, 16–32. 10.1128/mmbr.05015-11. [PubMed: 22390970]

38. Santoso CS, Li Z, Lal S, Yuan S, Gan KA, Agosto LM, Liu X, Pro SC, Sewell JA, Henderson A, et al. (2020). Comprehensive mapping of the human cytokine gene regulatory network. Nucleic Acids Res. 48, 12055–12073. 10.1093/nar/gkaa1055. [PubMed: 33179750]

39. Heinz S, Benner C, Spann N, Bertolino E, Lin YC, Laslo P, Cheng JX, Murre C, Singh H, and Glass CK (2010). Simple combinations of lineage-determining transcription factors prime cis-regulatory elements required for macrophage and B cell identities. Mol. Cell 38, 576–589. 10.1016/j.molcel.2010.05.004. [PubMed: 20513432]

40. Pogenberg V, Ogmundsdóttir MH, Bergsteinsdóttir K, Schepsky A, Phung B, Deineko V, Milewski M, Steingrímsson E, and Wilmanns M. (2012). Restricted leucine zipper dimerization and specificity of DNA recognition of the melanocyte master regulator MITF. Genes Dev. 26, 2647–2658. 10.1101/gad.198192.112. [PubMed: 23207919]

41. Grimm JB, English BP, Chen J, Slaughter JP, Zhang Z, Revyakin A, Patel R, Macklin JJ, Normanno D, Singer RH, et al. (2015). A general method to improve fluorophores for live-cell and single-molecule microscopy. Nat. Methods 12, 244–250. 10.1038/nmeth.3256. [PubMed: 25599551]

42. Blobel GA, Higgs DR, Mitchell JA, Notani D, and Young RA (2021). Testing the super-enhancer concept. Nat. Rev. Genet 22, 749–755. 10.1038/s41576-021-00398-w. [PubMed: 34480110]

43. Yoshino S, and Suzuki HI (2022). The molecular understanding of super-enhancer dysregulation in cancer. Nagoya J. Med. Sci 84, 216–229. 10.18999/nagjms.84.2.216. [PubMed: 35967935]

44. Tang SC, Vijayakumar U, Zhang Y, and Fullwood MJ (2022). Super-Enhancers, Phase-Separated Condensates, and 3D Genome Organization in Cancer. Cancers 14, 2866. 10.3390/cancers14122866. [PubMed: 35740532]

45. Lovén J, Hoke HA, Lin CY, Lau A, Orlando DA, Vakoc CR, Bradner JE, Lee TI, and Young RA (2013). Selective inhibition of tumor oncogenes by disruption of super-enhancers. Cell 153, 320–334. 10.1016/j.cell.2013.03.036. [PubMed: 23582323]

46. Du T, Wu Z, Wu Y, Liu Y, Song Y, and Ma L. (2023). CD44 Is Associated with Poor Prognosis of ccRCC and Facilitates ccRCC Cell Migration and Invasion through HAS1/MMP9. Biomedicines 11, 2077. 10.3390/biomedicines11072077. [PubMed: 37509716]

47. Foltyn M, Luger AL, Lorenz NI, Sauer B, Mittelbronn M, Harter PN, Steinbach JP, and Ronellenfitsch MW (2019). The physiological mTOR complex 1 inhibitor DDIT4 mediates therapy resistance in glioblastoma. Br. J. Cancer 120, 481–487. 10.1038/s41416-018-0368-3. [PubMed: 30745581]

48. Kortlever RM, Higgins PJ, and Bernards R. (2006). Plasminogen activator inhibitor-1 is a critical downstream target of p53 in the induction of replicative senescence. Nat. Cell Biol 8, 877–884. 10.1038/ncb1448. [PubMed: 16862142]

49. Gangwal K, Sankar S, Hollenhorst PC, Kinsey M, Haroldsen SC, Shah AA, Boucher KM, Watkins WS, Jorde LB, Graves BJ, and Lessnick SL (2008). Microsatellites as EWS/FLI response elements

in Ewing's sarcoma. Proc. Natl. Acad. Sci. USA 105, 10149–10154. 10.1073/pnas.0801073105. [PubMed: 18626011]

50. Guillon N, Tirode F, Boeva V, Zynovyev A, Barillot E, and Delattre O. (2009). The oncogenic EWS-FLI1 protein binds in vivo GGAA microsatellite sequences with potential transcriptional activation function. PLoS One 4, e4932. 10.1371/journal.pone.0004932. [PubMed: 19305498]
51. Riggi N, Knoechel B, Gillespie SM, Rheinbay E, Boulay G, Suvà ML, Rossetti NE, Boonseng WE, Oksuz O, Cook EB, et al. (2014). EWS-FLI1 utilizes divergent chromatin remodeling mechanisms to directly activate or repress enhancer elements in Ewing sarcoma. Cancer Cell 26, 668–681. 10.1016/j.ccell.2014.10.004. [PubMed: 25453903]
52. Tak YE, Boulay G, Lee L, Iyer S, Perry NT, Schultz HT, Garcia SP, Broye L, Horng JE, Rengarajan S, et al. (2022). Genome-wide functional perturbation of human microsatellite repeats using engineered zinc finger transcription factors. Cell Genom. 2, 100119. 10.1016/j.xgen.2022.100119. [PubMed: 35967079]
53. Ramšak M, Ramirez DA, Hough LE, Shirts MR, Vidmar S, Eleršić Filipić K, Anderluh G, and Jerala R. (2023). Programmable de novo designed coiled coil-mediated phase separation in mammalian cells. Nat. Commun 14, 7973. 10.1038/s41467-023-43742-w. [PubMed: 38042897]
54. Davis RB, Moosa MM, and Banerjee PR (2022). Ectopic biomolecular phase transitions: fusion proteins in cancer pathologies. Trends Cell Biol. 32, 681–695. 10.1016/j.tcb.2022.03.005. [PubMed: 35484036]
55. McWhirter JR, Galasso DL, and Wang JY (1993). A coiled-coil oligomerization domain of Bcr is essential for the transforming function of Bcr-Abl oncoproteins. Mol. Cell Biol 13, 7587–7595. 10.1128/mcb.13.12.7587-7595.1993. [PubMed: 8246975]
56. Kummalue T, Lou J, and Friedman AD (2002). Multimerization via its myosin domain facilitates nuclear localization and inhibition of core binding factor (CBF) activities by the CBFbeta-smooth muscle myosin heavy chain myeloid leukemia oncoprotein. Mol. Cell Biol 22, 8278–8291. 10.1128/mcb.22.23.8278-8291.2002. [PubMed: 12417730]
57. Reiter A, Walz C, Watmore A, Schoch C, Blau I, Schlegelberger B, Berger U, Telford N, Aruliah S, Yin JA, et al. (2005). The t(8;9)(p22;p24) is a recurrent abnormality in chronic and acute leukemia that fuses PCM1 to JAK2. Cancer Res. 65, 2662–2667. 10.1158/0008-5472.Can-04-4263. [PubMed: 15805263]
58. Ishiguro M, Iwasaki H, Ohjimi Y, and Kaneko Y. (2004). Establishment and characterization of a renal cell carcinoma cell line (FU-UR-1) with the reciprocal ASPL-TFE3 fusion transcript. Oncol. Rep 11, 1169–1175. [PubMed: 15138551]
59. ISHIGURO M, FUKUSHIGE T, and IWASAKI H. (2023). Establishment and Characterization of a TFE3-rearranged Renal Cell Carcinoma Cell Line (FU-UR-2) With the PRCC-TFE3 Fusion Transcript. Anticancer Res. 43, 3463–3470. 10.21873/anticanres.16522. [PubMed: 37500159]
60. Sebastian R, Hosogane EK, Sun EG, Tran AD, Reinhold WC, Burkett S, Sturgill DM, Gudla PR, Pommier Y, Aladjem MI, and Oberdoerffer P. (2020). Epigenetic Regulation of DNA Repair Pathway Choice by MacroH2A1 Splice Variants Ensures Genome Stability. Mol. Cell 79, 836–845.e7. 10.1016/j.molcel.2020.06.028. [PubMed: 32649884]
61. Sergé A, Bertaux N, Rigneault H, and Marguet D. (2008). Dynamic multiple-target tracing to probe spatiotemporal cartography of cell membranes. Nat. Methods 5, 687–694. 10.1038/nmeth.1233. [PubMed: 18604216]
62. Heckert A, Dahal L, Tjian R, and Darzacq X. (2022). Recovering mixtures of fast-diffusing states from short single-particle trajectories. Elife 11, e70169. 10.7554/eLife.70169. [PubMed: 36066004]
63. Schneider CA, Rasband WS, and Eliceiri KW (2012). NIH Image to ImageJ: 25 years of image analysis. Nat. Methods 9, 671–675. [PubMed: 22930834]
64. Stringer C, and Pachitariu M. (2024). Cellpose3: one-click image restoration for improved cellular segmentation. Preprint at bioRxiv. 10.1101/2024.02.10.579780.
65. Stirling DR, Swain-Bowden MJ, Lucas AM, Carpenter AE, Cimini BA, and Goodman A. (2021). CellProfiler 4: improvements in speed, utility and usability. BMC Bioinf. 22, 433. 10.1186/s12859-021-04344-9.

66. R Core Team (2018). R: A Language and Environment for Statistical Computing (Vienna, Austria: R Foundation for Statistical Computing). https://www.R-project.org/.

67. Chen S, Zhou Y, Chen Y, and Gu J. (2018). fastp: an ultra-fast all-in-one FASTQ preprocessor. Bioinformatics 34, i884–i890. 10.1093/bioinformatics/bty560. [PubMed: 30423086]

68. Chen S. (2023). Ultrafast one-pass FASTQ data preprocessing, quality control, and deduplication using fastp. Imeta 2, e107. 10.1002/imt2.107. [PubMed: 38868435]

69. Patro R, Duggal G, Love MI, Irizarry RA, and Kingsford C. (2017). Salmon provides fast and bias-aware quantification of transcript expression. Nat. Methods 14, 417–419. 10.1038/nmeth.4197. [PubMed: 28263959]

70. Love MI, Huber W, and Anders S. (2014). Moderated estimation of fold change and dispersion for RNA-seq data with DESeq2. Genome Biol. 15, 550. 10.1186/s13059-014-0550-8. [PubMed: 25516281]

71. Gu Z, Eils R, and Schlesner M. (2016). Complex heatmaps reveal patterns and correlations in multidimensional genomic data. Bioinformatics 32, 2847–2849. 10.1093/bioinformatics/btw313. [PubMed: 27207943]

72. Gu Z. (2022). Complex heatmap visualization. Imeta 1, e43. 10.1002/imt2.43. [PubMed: 38868715]

73. Mootha VK, Lindgren CM, Eriksson KF, Subramanian A, Sihag S, Lehar J, Puigserver P, Carlsson E, Ridderstråle M, Laurila E, et al. (2003). PGC-1alpha-responsive genes involved in oxidative phosphorylation are coordinately downregulated in human diabetes. Nat. Genet 34, 267–273. 10.1038/ng1180. [PubMed: 12808457]

74. Subramanian A, Tamayo P, Mootha VK, Mukherjee S, Ebert BL, Gillette MA, Paulovich A, Pomeroy SL, Golub TR, Lander ES, and Mesirov JP (2005). Gene set enrichment analysis: a knowledge-based approach for interpreting genome-wide expression profiles. Proc. Natl. Acad. Sci. USA 102, 15545–15550. 10.1073/pnas.0506580102. [PubMed: 16199517]

75. Hänzelmann S, Castelo R, and Guinney J. (2013). GSVA: gene set variation analysis for microarray and RNA-seq data. BMC Bioinf. 14, 1–5. 10.1186/1471-2105-14-7.

76. Liberzon A, Subramanian A, Pinchback R, Thorvaldsdóttir H, Tamayo P, and Mesirov JP (2011). Molecular signatures database (MSigDB) 3.0. Bioinformatics 27, 1739–1740. 10.1093/bio-informatics/btr260. [PubMed: 21546393]

77. Liberzon A, Birger C, Thorvaldsdóttir H, Ghandi M, Mesirov JP, and Tamayo P. (2015). The Molecular Signatures Database (MSigDB) hallmark gene set collection. Cell Syst. 1, 417–425. 10.1016/j.cels.2015.12.004. [PubMed: 26771021]

78. Dobin A, Davis CA, Schlesinger F, Drenkow J, Zaleski C, Jha S, Batut P, Chaisson M, and Gingeras TR (2013). STAR: ultrafast universal RNA-seq aligner. Bioinformatics 29, 15–21. 10.1093/bioinformatics/bts635. [PubMed: 23104886]

79. Pohl A, and Beato M. (2014). bwtool: a tool for bigWig files. Bioinformatics 30, 1618–1619. 10.1093/bioinformatics/btu056. [PubMed: 24489365]

80. Mayakonda A, and Westermann F. (2024). Trackplot: a fast and light-weight R script for epigenomic enrichment plots. Bioinform. Adv 4, vbae031. 10.1093/bioadv/vbae031. [PubMed: 38476298]

81. Langmead B, and Salzberg SL (2012). Fast gapped-read alignment with Bowtie 2. Nat. Methods 9, 357–359. 10.1038/nmeth.1923. [PubMed: 22388286]

82. Picard T. (Accessed: 2018/02/21; version 2.17.8). Picard toolkit. Broad Institute, GitHub repository.

83. Zhang Y, Liu T, Meyer CA, Eeckhoute J, Johnson DS, Bernstein BE, Nusbaum C, Myers RM, Brown M, Li W, and Liu XS (2008). Model-based analysis of ChIP-Seq (MACS). Genome Biol. 9, R137. 10.1186/gb-2008-9-9-r137. [PubMed: 18798982]

84. Zhu LJ (2013). Integrative analysis of ChIP-chip and ChIP-seq dataset. Methods Mol. Biol. 1067, 105–124. 10.1007/978-1-62703-607-8_8.

85. Ramírez F, Ryan DP, Grüning B, Bhardwaj V, Kilpert F, Richter AS, Heyne S, Dündar F, and Manke T. (2016). deepTools2: a next generation web server for deep-sequencing data analysis. Nucleic Acids Res. 44, W160–W165. 10.1093/nar/gkw257. [PubMed: 27079975]

86. Whyte WA, Orlando DA, Hnisz D, Abraham BJ, Lin CY, Kagey MH, Rahl PB, Lee TI, and Young RA (2013). Master transcription factors and mediator establish super-enhancers at key cell identity genes. Cell 153, 307–319. 10.1016/j.cell.2013.03.035. [PubMed: 23582322]

87. Hulsen T. (2022). DeepVenn – a web application for the creation of area-proportional Venn diagrams using the deep learning framework Tensor-flow. Preprint at arXiv. 10.48550/arXiv.2210.04597.

88. Zhang T, Wu YC, Mullane P, Ji YJ, Liu H, He L, Arora A, Hwang HY, Alessi AF, Niaki AG, et al. (2018). FUS Regulates Activity of MicroRNA-Mediated Gene Silencing. Mol. Cell 69, 787–801.e8. 10.1016/j.molcel.2018.02.001. [PubMed: 29499134]

89. McSwiggen DT, Liu H, Tan R, Puig SA, Akella LB, Berman R, Bretan M, Chen H, Darzacq X, Ford K, et al. (2023). A High-Throughput Platform for Single-Molecule Tracking Identifies Drug Interaction and Cellular Mechanisms (Cold Spring Harbor Laboratory).

90. Corces MR, Trevino AE, Hamilton EG, Greenside PG, Sinnott-Armstrong NA, Vesuna S, Satpathy AT, Rubin AJ, Montine KS, Wu B, et al. (2017). An improved ATAC-seq protocol reduces background and enables interrogation of frozen tissues. Nat. Methods 14, 959–962. 10.1038/nmeth.4396. [PubMed: 28846090]

91. So CL, Robitaille M, Sadras F, McCullough MH, Milevskiy MJG, Goodhill GJ, Roberts-Thomson SJ, and Monteith GR (2024). Cellular geometry and epithelial-mesenchymal plasticity intersect with PIEZO1 in breast cancer cells. Commun. Biol 7, 467. 10.1038/s42003-024-06163-z. [PubMed: 38632473]

92. Cai D, Feliciano D, Dong P, Flores E, Gruebele M, Porat-Shliom N, Sukenik S, Liu Z, and Lippincott-Schwartz J. (2019). Phase separation of YAP reorganizes genome topology for long-term YAP target gene expression. Nat. Cell Biol 21, 1578–1589. 10.1038/s41556-019-0433-z. [PubMed: 31792379]

93. Song L, Yao X, Li H, Peng B, Boka AP, Liu Y, Chen G, Liu Z, Mathias KM, Xia L, et al. (2022). Hotspot mutations in the structured ENL YEATS domain link aberrant transcriptional condensates and cancer. Mol. Cell 82, 4080–4098.e12. 10.1016/j.molcel.2022.09.034. [PubMed: 36272410]

94. Lyons H, Veettil RT, Pradhan P, Fornero C, De La Cruz N, Ito K, Eppert M, Roeder RG, and Sabari BR (2023). Functional partitioning of transcriptional regulators by patterned charge blocks. Cell 186, 327–345.e28. 10.1016/j.cell.2022.12.013. [PubMed: 36603581]

95. Patel A, Lee HO, Jawerth L, Maharana S, Jahnel M, Hein MY, Stoy-nov S, Mahamid J, Saha S, Franzmann TM, et al. (2015). A Liquid-to-Solid Phase Transition of the ALS Protein FUS Accelerated by Disease Mutation. Cell 162, 1066–1077. 10.1016/j.cell.2015.07.047. [PubMed: 26317470]

Highlights

- TFE3 FOs form transcriptionally active biomolecular condensates
- The structured coiled-coil domains of TFE3 FOs are required for condensate formation
- TFE3 FOs condensates promote cell proliferation and migration
- TFE3 FOs condensates remodel chromatin landscape and oncogenic gene expression

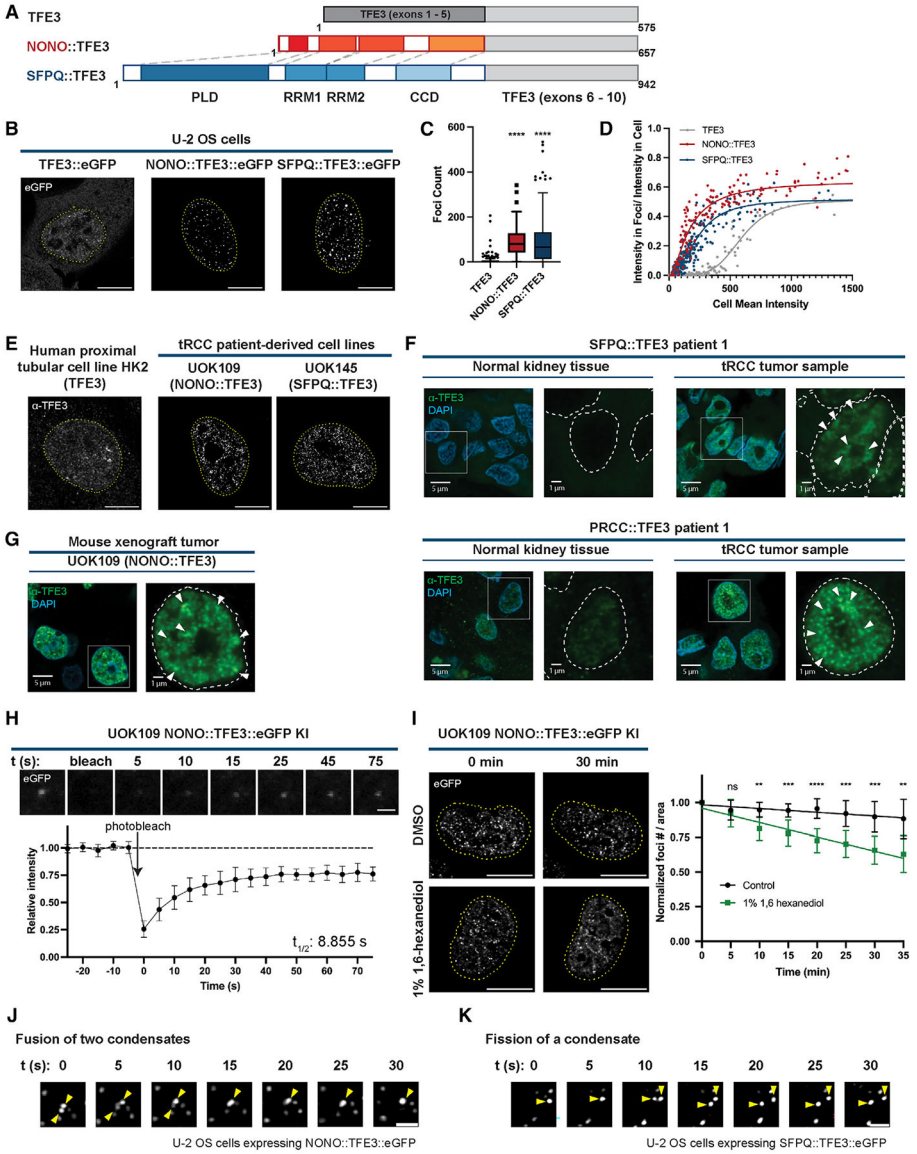

Figure 1. TFE3 FOs form biomolecular condensates

(A) Domain illustrations of TFE3, NONO::TFE3, and SFPQ::TFE3.

(B) Representative images of TFE3::eEFP, NONO::TFE3::eGFP, and SFPQ::TFE3::eGFP expression in U-2 OS cells. Scale bars, 5 μm.

(C) Quantification of eGFP foci count (prominence = 600) in each transfected U-2 OS cell shown in (B) that has a mean nuclear intensity below 600 a.u. Each data point indicates one cell (n = 115–255 cells).

(D) Plot showing the fraction of in-foci fluorescence intensity as a function of mean nuclear fluorescence intensity. Each data point indicates one cell (n = 136–274 cells).

(E) Representative immunofluorescence (IF) images against the C terminus of TFE3 in HK2, UOK109, and UOK145 cells. Scale bars, 5 μm.

(F) Representative IF images against the C terminus of TFE3 (green) of matched normal kidney tissue and tRCC tumor sample from patients. Arrows indicating foci/condensates. Scale bars, 5 μm and 1 μm (zoomed-in image).
(G) Representative IF images against the C-terminal of TFE3 (green) of a xenograft of UOK109 cells (NONO::TFE3) in NOD scid gamma mouse. Arrows indicating foci/condensates. Scale bars, 5 μm and 1 μm (zoomed-in image).
(H) Representative images of NONO::TFE3::eGFP knockin (KI) foci in UOK109 cells before and after photobleaching in FRAP experiment. Average relative intensity of each foci (n = 10 foci) plotted against time.
(I) Representative images of NONO::TFE3::eGFP in cell nucleus (dotted circle) of UOK109 NONO::TFE3::eGFP KI cells before and after DMSO or 1,6-hexanediol treatment. Scale bars, 10 μm. Graph of average normalized number of foci/nuclear area in each field of view (n = 8 fields of view).
(J) Representative images of a fusion of two condensates in a U-2 OS cell expressing NONO::TFE3::eGFP. Scale bars, 1 μm.
(K) Representative images of fission of one condensate in a U-2 OS cell expressing SFPQ::TFE3::eGFP. Scale bars, 1 μm. For (C) and (D), mean ± SEM; for (H) and (I), mean ± SD. ns, $p > 0.05$, **$p \leq 0.01$, ***$p \leq 0.001$, ****$p \leq 0.0001$ (one-way ANOVA) (C), (unpaired t test) (I). See also Figure S1 and Videos S1-S7.

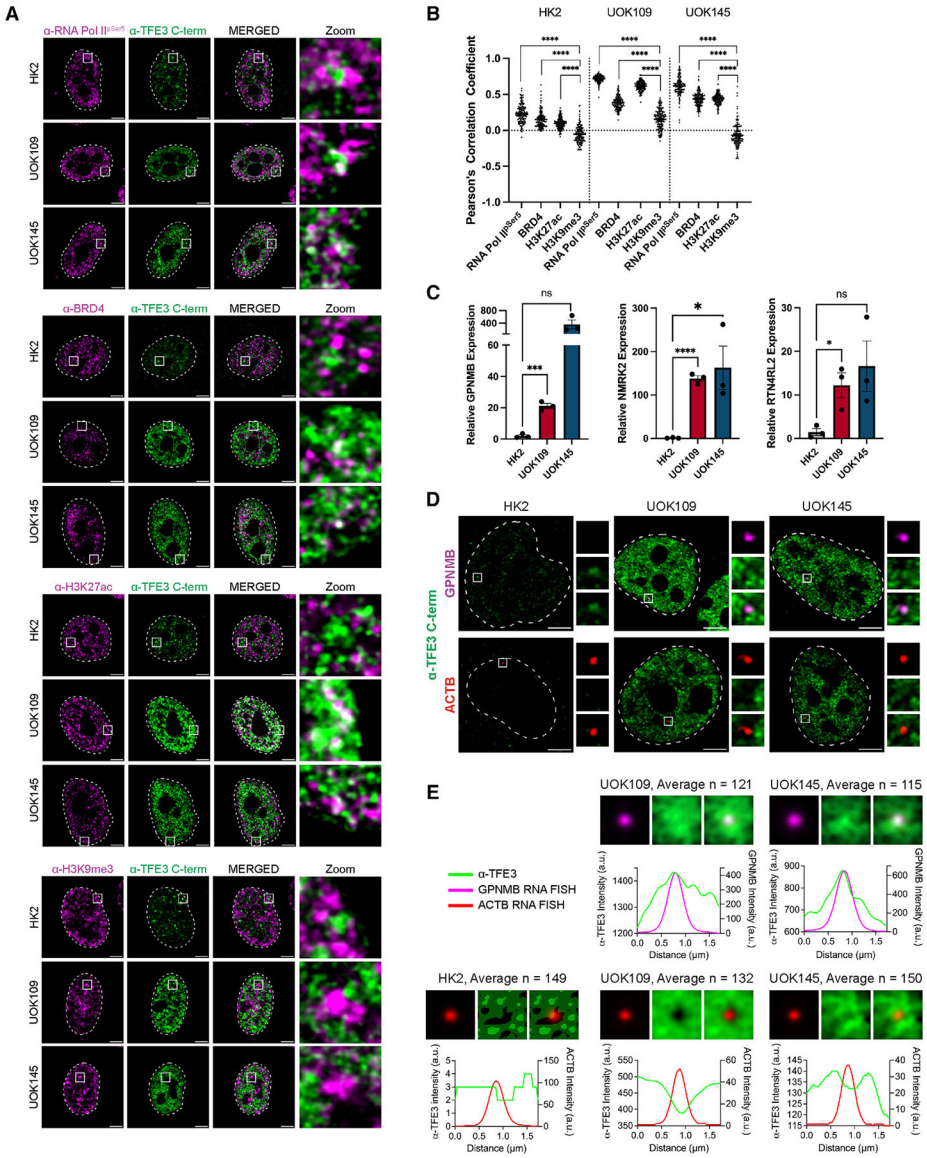

Figure 2. TFE3 FO condensates are associated with active transcription

(A) Representative images of co-IF against the C terminus of TFE3 (green) and indicated proteins (magenta) in HK2, UOK109, and UOK145 cells. Scale bars, 5 μm. Zoomed-in images to the right.

(B) Quantification of Pearson's colocalization coefficients per cell from co-IF in (A) (n = 150 cells for each cell line in each condition).

(C) Relative mRNA expression of *GPNMB*, *NMRK2*, and *RTN4RL2* (normalized to *GAPDH*) in HK2, UOK109, and UOK145 cell lines (n = 3 biological replicates).

(D) Representative images of simultaneous IF against the C terminus of TFE3 (green) and ice-FISH against *GPNMB* (magenta) or *ACTB* (red). Scale bars, 5 μm.

(E) Line plots of TFE3 (green line, left) and *GPNMB* (magenta line, right) or *ACTB* (red line, right) average intensities of all images centered at either *GPNMB* or *ACTB* point

signal. For (B) and (C), mean ± SEM, *$p \leq 0.05$, ****$p \leq 0.0001$, one-way ANOVA. See also Figure S2.

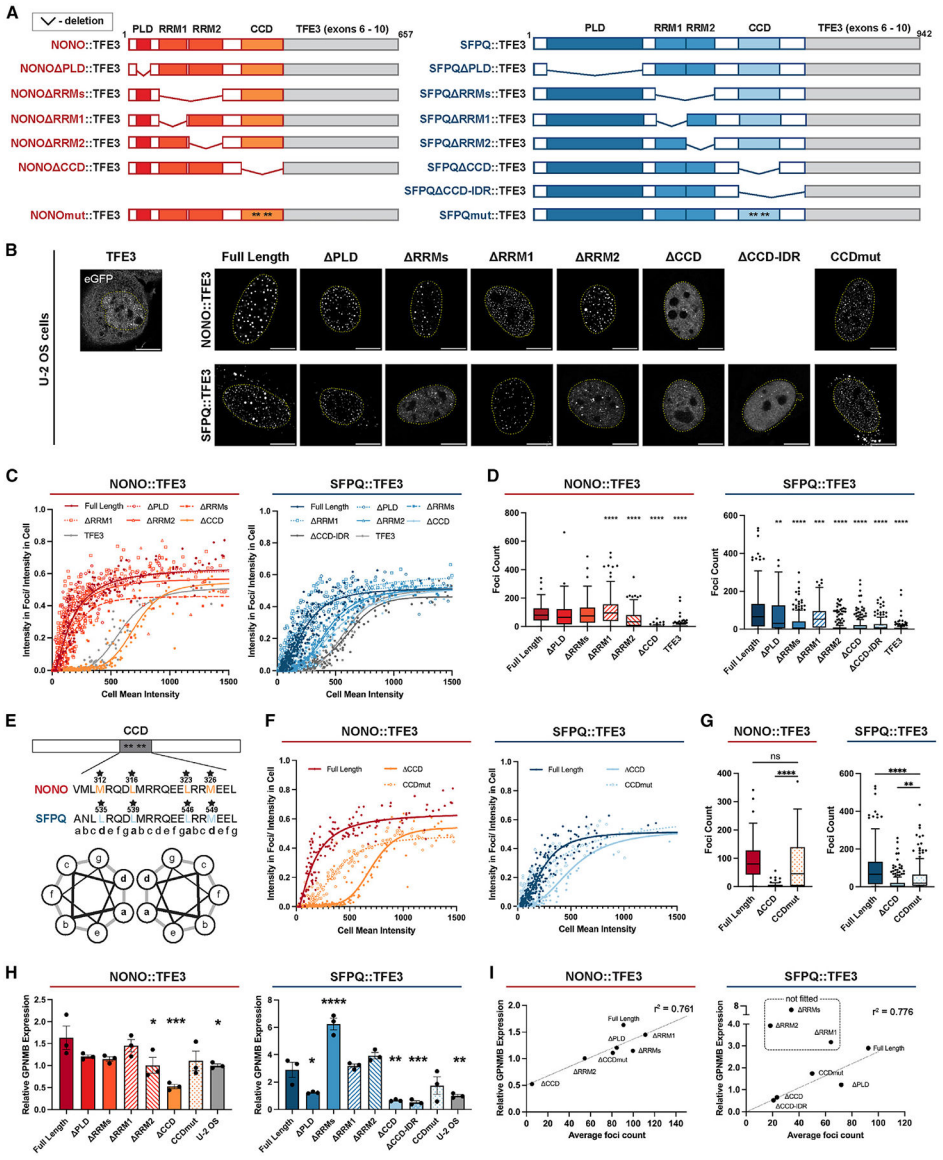

Figure 3. CCDs of NONO and SFPQ are important for TFE3 FO condensate formation

(A) Illustration of NONO::TFE3 and SFPQ::TFE3 fusion and their respective domain deletion and mutation.

(B) Representative images of U-2 OS cells transfected with indicated constructs with an eGFP tag. Scale bars, 10 μm.

(C) Plots showing fraction of in-foci fluorescence intensity as a function of mean nuclear fluorescence intensity in U-2 OS cells transfected with indicated constructs. Each dot indicates one cell (n = 104–274 cells).

(D) Quantification of eGFP foci counts (prominence = 600) in each transfected U-2 OS cell shown in (B) that has a mean nuclear intensity below 600 a.u. Each data point indicates one cell (n = 80–204 cells).

(E) Illustration of NONOmut::TFE3 and SFPQmut::TFE3 mutants. The helical wheel represents the knobs and holes heptad for NONO and SFPQ antiparallel coiled-coil

interaction. Sequence alignment of the coiled-coil interaction motifs is shown. Coiled-coil interacting amino acids (starred) are mutated to alanine.

(F) Plots showing fraction of in-foci fluorescence intensity as a function of mean nuclear fluorescence intensity. Each data point indicates one cell (NONO set *n* range = 133–175 cells; SFPQ set *n* range = 184–274).

(G) Quantification of foci count (prominence = 600) in each transfected U-2 OS cell shown in (F) that has a mean nuclear intensity below 600 a.u. Each data point indicates one cell (NONO set *n* range = 95–130 cells; SFPQ set *n* range = 170–255 cells).

(H) Relative mRNA expression of *GPNMB* (normalized to *GAPDH*) in U-2 OS cell transfections.

(I) Graphs of relative *GPNMB* expression against average foci count of indicated constructs. ΔRRMs, ΔRRM1, and ΔRRM2 of SFPQ were excluded from linear regression. For (B), (G), and (H), mean ± SEM. ns $p > 0.05$, *$p \leq 0.05$, **$p \leq 0.01$, ***p Δ 0.001, ****$p \leq 0.0001$, one-way ANOVA. See also Figure S3.

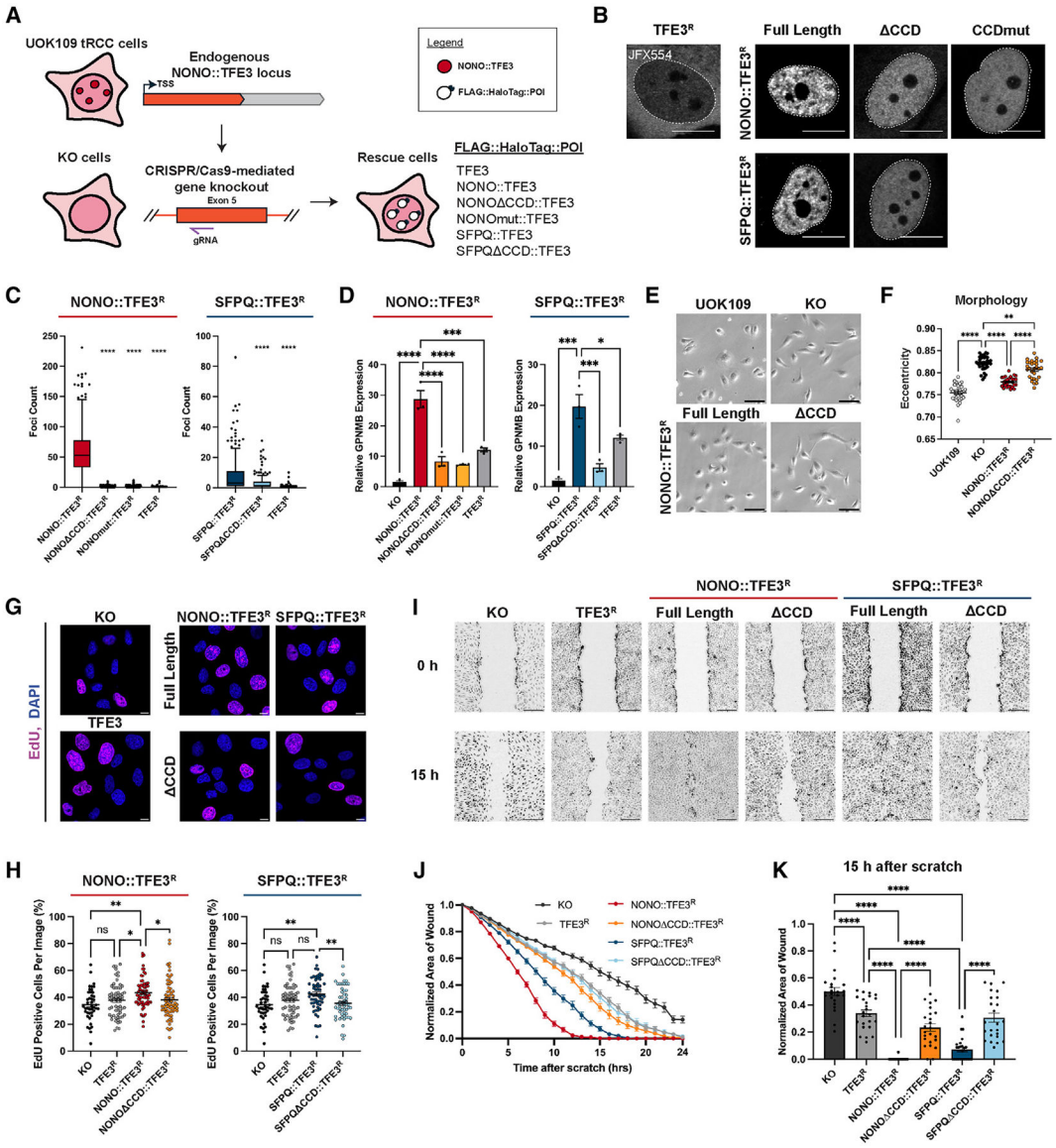

Figure 4. TFE3 FO condensates mediate cell proliferation and migration in tRCC cells

(A) Illustration of the generation of the knockout (KO)-rescue model.

(B) Representative live-cell images of KO-rescue cells expressing the indicated POI and stained with JFX554 HaloTag ligand. Scale bars, 10 μm.

(C) Quantification of foci count (prominence = 500) in each rescue cell shown in (B). Each data point indicates one cell (n = 197–448 cells).

(D) Relative mRNA expression of *GPNMB* (normalized to *GAPDH*) in rescue cells shown in (B) (n = 3 biological replicates).

(E) Representative bright-field images of UOK109 KO cells rescued with indicated constructs. Scale bars, 100 μm.

(F) Quantification of eccentricity (measurement of circularity) from images in (E). Each data point indicates the mean eccentricity of cells in one image (n = 29–35 fields of view).

(G) Representative images of 5-ethynyl 2′-deoxyuridine (EdU) incorporation for 1 h in UOK109 KO-rescue cells. Scale bars, 10 μm.
(H) Quantification of percent EdU-positive cells per image in (G) (n = 43–68 fields of view).
(I) Representative bright-field images of scratches at 0 h and after 15 h made on confluent UOK109 KO-rescue cells pre-treated with aphidicolin to inhibit cell proliferation. Scale bars, 200 μm.
(J) Fraction area of wound of KO-rescue cell lines every 1 h from 0 to 24 h after scratch from 24 fields of view for each cell line.
(K) Fraction area of wound of KO-rescue cell lines 15 h after scratch (n = 3 biological replicates, 8 fields of view each). For (C), (D), (F), and (K), mean ± SEM. ns $p > 0.05$, *$p \leq 0.05$, **$p \leq 0.01$, ***$p \leq 0.001$, ****$p \leq 0.0001$, one-way ANOVA. See also Figure S4.

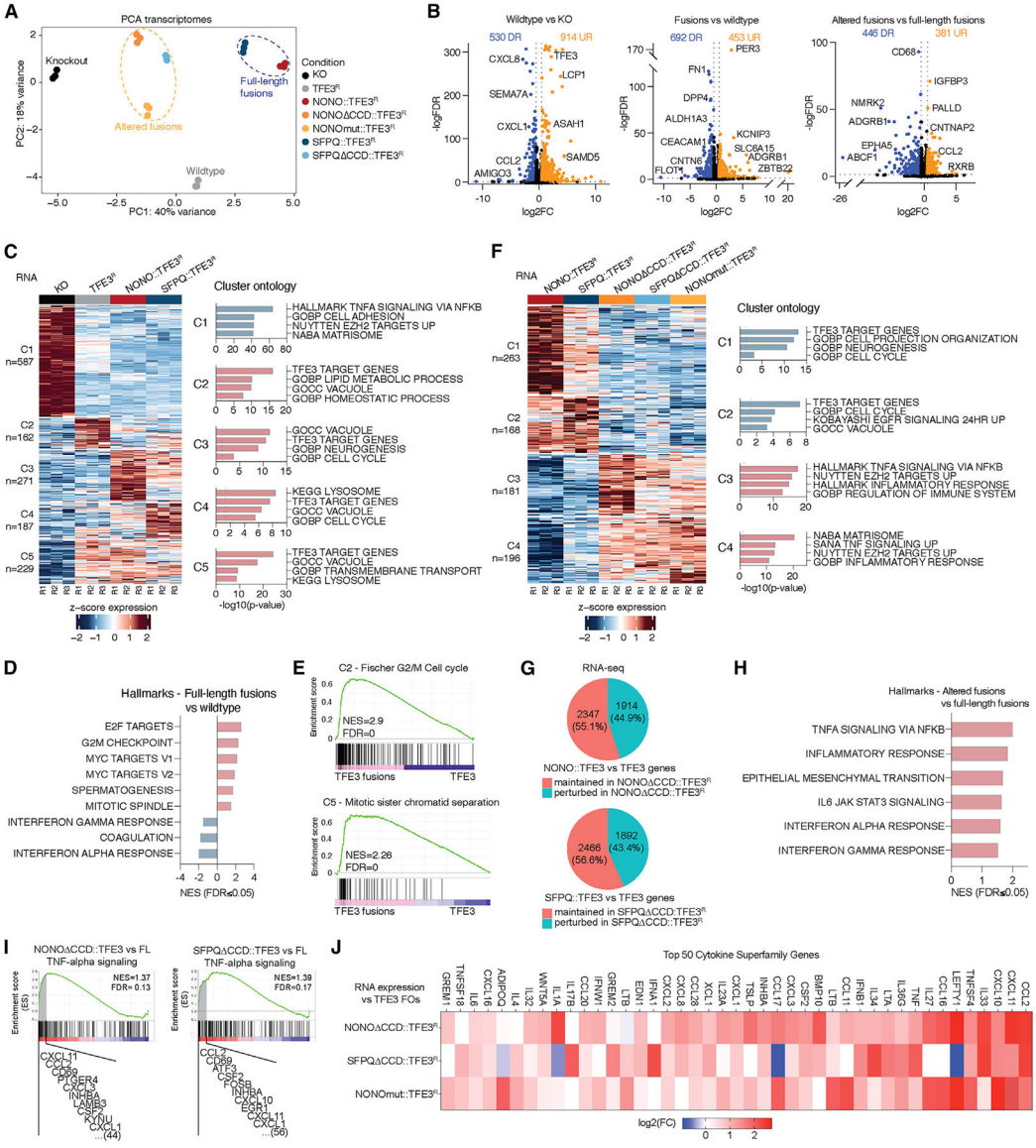

Figure 5. TFE3 FO condensates regulate oncogenic transcriptional programs in tRCC cells

(A) PCA of all transcriptomes from control KO and gene-overexpressing UOK109 cells (n = 3 biological replicates). R, rescue.

(B) Volcano plots of transcriptomic changes in indicated differential analyses. DRG, downregulated gene; URG, upregulated gene.

(C) K-means (n = 5) clustering heatmap of differential gene expression using the indicated samples (n = 3 biological replicates) with associated top 4 gene ontologies per cluster using an aggregate of genesets (H, C2, C3, C5) from the Molecular Signatures Database (MSigDB, Broad Institute).

(D) Bar plots showing all significant ($p < 0.05$) transcriptomic signatures from the MSigDB Hallmarks and their normalized enrichment score (NES) when comparing full-length NONO:: or SFPQ::TFE3 (full-length fusions) versus wild-type TFE3.

(E) Enrichment plot of indicated molecular signatures derived from gene set enrichment analysis (GSEA) of TFE3 fusion versus wild-type TFE3.
(F) K-means ($n = 4$) clustering heatmap of differential gene expression using the indicated samples ($n = 3$ biological replicates) with associated top 4 gene ontologies per cluster using an aggregate of genesets (H, C2, C3, C5) from the MSigDB.
(G) Venn diagrams depicting the percentages of differentially expressed genes in TFE3 FOs versus TFE3 that are perturbed and maintained by CCD alterations ($p < 0.05$, log2FC < 0.1).
(H) Bar plots showing all significant ($p < 0.05$) transcriptomic signatures from the MSigDB Hallmarks and their NES when comparing NONOΔCCD::, NONOmut::, or SFPQΔCCD::TFE3 (altered fusions) versus full-length TFE3 fusions.
(I) GSEA leading edge analysis of TNF-α signaling pathway in the indicated transcriptomic conditions.
(J) The RNA expression of top 50 significantly deregulated cytokine genes for the indicated conditions. See also Figure S5.

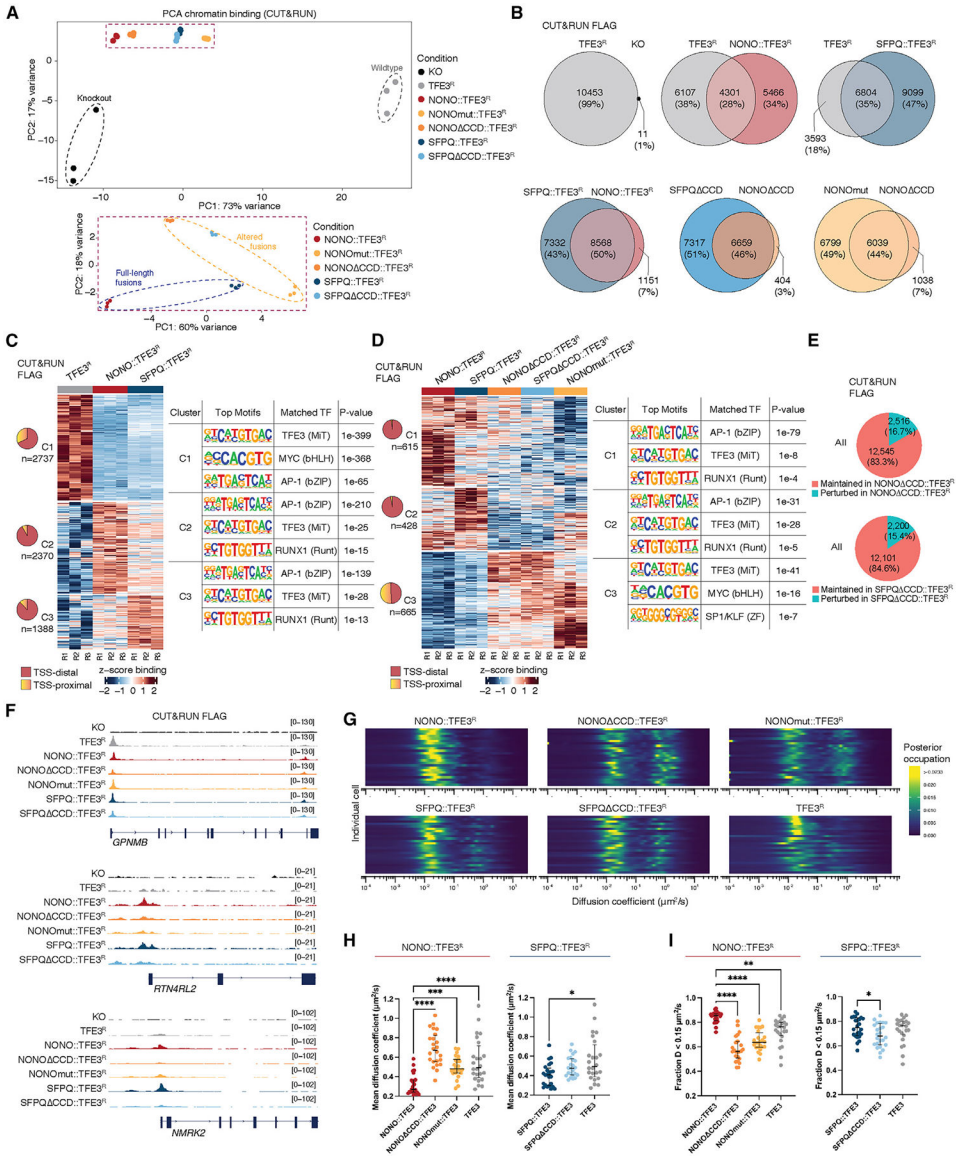

Figure 6. The CCDs of TFE3 FOs are critical for genome-wide reprogramming of canonical TFE3 cistrome

(A) PCA of all genome binding sites (anti-FLAG CUT&RUN) from KO and rescue UOK109 cells (upper panel) and separate analysis highlighting binding profiles of full-length and altered TFE3 fusions (lower panel). All datasets are $n = 3$ biological replicates.

(B) Venn diagrams showing peak overlap counts and associated absolute percentages in indicated CUT&RUN samples.

(C and D) K-means ($n = 3$) clustering of FLAG CUT&RUN binding sites of the indicated samples with associated relative distance to TSSs (pie charts) and top 3 MEME TF motif enrichment analysis with best matched TF per cluster.

(E) Venn diagrams depicting the percentages of differentially bound peaks in FLAG::TFE3 FOs versus FLAG::TFE3 that are affected (perturbed) and unaffected (maintained) by CCD alterations ($p < 0.05$, log2FC < 0.1).

(F) Examples of binding profiles from the indicated samples for canonical or novel TFE3 fusion transcriptional targets.

(G) Heatmap representation of posterior occupations for a state array evaluated on NONO::TFE3, NONOΔCCD::TFE3, NONOmut::TFE3, SFPQ::TFE3, SFPQΔCCD::TFE3, TFE3 in cell nuclei. Each horizontal line represents a nucleus (n = 24 cells from 3 biological replicates).

(H) Quantification of the mean diffusion coefficients of the data in (F). *p < 0.05, ***p < 0.001, ****p < 0.0001, Kruskal-Wallis test.

(I) Quantification of the fraction of trajectories of the data in (G) with diffusion coefficients less than 0.15 $\mu m^2/s$. *p < 0.05, **p < 0.01, ****p < 0.0001, Kruskal-Wallis test. See also Figure S6, Table S1, and Videos S8-S13.

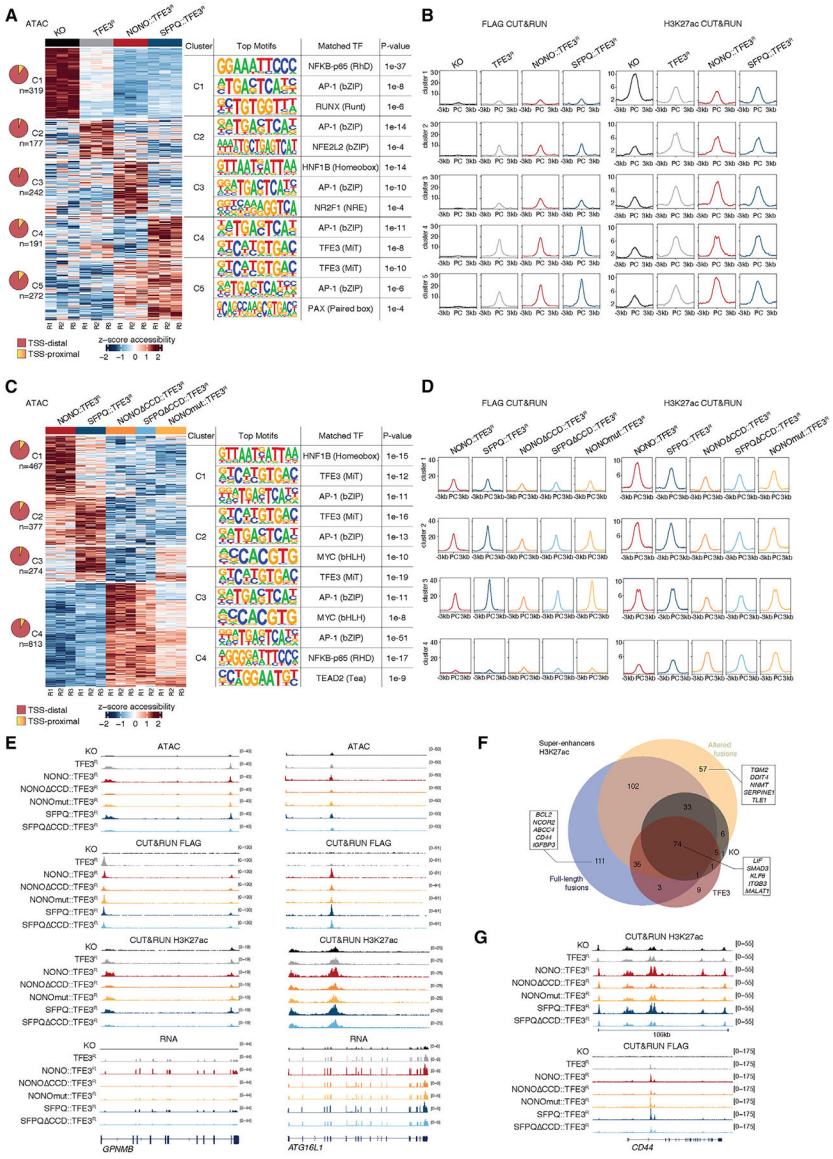

Figure 7. TFE3 FO condensates remodel chromatin landscape and enhancer activity in tRCC cells

(A) K-means (n = 5) clustering of differential chromatin accessible sites (ATAC-seq) of the indicated samples with associated relative distance to TSSs (pie charts) and top 3 MEME TF motif enrichment analysis with best matched TF per cluster (table).

(B) Integration of FLAG and H3K27ac CUT&RUN metaprofiles for the indicated samples (merged triplicate signal) based on ATAC-seq clusters from (A).

(C) K-means (n = 4) clustering of differential chromatin accessible sites (ATAC-seq) of indicated samples with associated relative distance to TSSs (pie charts) and top 3 MEME TF motifs with best matched TF per cluster.

(D) Integration of FLAG and H3K27ac CUT&RUN metaprofiles for the indicated samples on ATAC-seq clusters from (C).

(E) Examples of integrated chromatin landscape and transcriptional profiles from the indicated samples.

(F) Venn diagrams showing overlap of super-enhancer (SE) counts in indicated individual or grouped samples.
(G) Trackplot of CUT&RUN data showing the CD44-associated SE cluster. See also Figures S7 and S8 and Table S2.

KEY RESOURCES TABLE

REAGENT or RESOURCE	SOURCE	IDENTIFIER
Antibodies		
anti-BRD4 antibody	Cell Signaling	Cat# 63759; RRID:AB_3083075
anti-TFE3 antibody	Abcam	Cat# AB93808; RRID:AB_10563130
anti-TFE3 antibody	Millipore Sigma	Cat# HPA023881; RRID:AB_1857931
anti-FLAG M2 antibody	Millipore Sigma	Cat# F3165-.2MG; RRID:AB_259529
anti-β-actin antibody	Millipore Sigma	Cat# A1978; RRID:AB_476692
IRdye 800CW goat-anti-rabbit	LI-COR Biosciences	Cat# 926–32211; RRID:AB_621843
IRdye 800CW donkey-anti-mouse	LI-COR Biosciences	Cat# 926–32212; RRID:AB_621847
IRdye 680RD goat anti-mouse	LI-COR Biosciences	Cat# 926–68070; RRID:AB_10956588
anti-RNA Pol II Ser5P antibody	Abcam	Cat# ab5408; RRID:AB_304868
anti-RNA Pol II Ser2P antibody	Active Motif	Cat# 61083; RRID:AB_2687450
anti-H3K27ac antibody	Active Motif	Cat# 39685; RRID:AB_2793305
anti-H3K9me3 antibody	Active Motif	Cat# 39285; RRID:AB_2935892
Goat anti-Mouse IgG (H + L) Cross-Adsorbed Secondary Antibody, Alexa Fluor 568	Thermo Fisher	Cat# A11031; RRID:AB_144696
Goat anti-Mouse IgG (H + L) Cross-Adsorbed Secondary Antibody, Alexa Fluor 647	Thermo Fisher	Cat# A21235; RRID:AB_2535804
Goat anti-Rabbit IgG (H + L) Cross-Adsorbed Secondary Antibody, Alexa Fluor 488	Thermo Fisher	Cat# A11034; RRID:AB_2576217
Goat anti-Rat IgG (H + L) Cross-Adsorbed Secondary Antibody, Alexa Fluor 647	Thermo Fisher	Cat# A21247; RRID:AB_141778
Biological samples		
Deidentified frozen tRCC patient tissue (SFPQ::TFE3 patient 1 and PRCC::TFE3 patient 1)	Lang M. et al.[6]	N/A
Deidentified frozen tRCC patient tissue (SFPQ::TFE3 patient 2)	Johns Hopkins Hospital Repository	IRB number: MOD00005088
Chemicals, peptides, and recombinant proteins		
Dulbecco's Modified Eagle's Medium (DMEM)	Corning	15-013-CV
DMEM/F12 50:50 Mix	Corning	15-090-CV
EMEM with L-Glutamine	Quality Biological	112-018-101
FluoroBrite DMEM	Gibco	A1896701
Roswell Park Memorial Institute (RPMI) 1640	Corning	10-040-CM
FBS, Tet system approved, USDA-approved regions	Gibco	A4736401
Fetal bovine serum (FBS)	Gibco	26140079
GlutaMAX Supplement	Thermo Fisher	35050061
Mem Non Essential Amino Acids Solution (100X)	Thermo Fisher	11140050
Penicillin-Streptomycin (10,000 U/mL)	Thermo Fisher	15140122
Sodium pyruvate (100 mM)	Thermo Fisher	11360070
ATCC TransfeX	ATCC	ACS-4005
Lipofectamine 3000 Transfection Reagent	ThermoFisher	L3000015
Aphidicolin	Cell Signaling	32774

REAGENT or RESOURCE	SOURCE	IDENTIFIER
Doxycycline hyclate	Sigma-Aldrich	D9891-1G
G418 sulfate	Corning	30-234-CR
Hoechst 33342	Thermo Scientific	62249
Matrigel	Corning	354234
1,6-hexanediol	Sigma-Aldrich	88571
Igepal® CA-630	Sigma Aldrich	56741-50ML-F
Sodium deoxycholate	Sigma Aldrich	30970-25G
cOmplete™ Mini Protease Inhibitor Cocktail	Sigma Aldrich	11836170001
Anti-DYKDDDDK Magnetic Agarose	Thermo Scientific	A36797
JF549-HaloTag ligand	Janelia Materials; Grimm et al.[41]	N/A
JFX554-HaloTag ligand	Janelia Materials; Grimm et al.[41]	N/A
RNeasy Lysis Buffer	Qiagen	79216
Q5 High-Fidelity 2X Master Mix	NEB	M0492
HiFi DNA Assembly	NEB	E2621X
Critical commercial assays		
GeneJET Genomic DNA Purification Kit	Thermo Scientific	K0721
Monarch DNA Gel Extraction Kit	NEB	T1020S
4-12% Surepage Bis-Tris gel	GenScript	M00654
Odyssey Nitrocellulose Membrane, 0.22 μm	LI-COR Biosciences	926–31090
Click-iT EdU Proliferation assay kit	Thermo Fisher Scientific	C11008
RNeasy Mini Kit	Qiagen	74104
RNase-Free DNase Set	Qiagen	79254
Illumina Tagment DNA Enzyme and Buffer Kit	Illumina	20034197
Zymo DNA Clean and Concentrator-5 Kit	Zymo	D4014
2x NEBNext Q5 Hotstart HiFi PCR Master Mix	NEB	M0543L
Epicypher's CUTANA CUT&RUN kit v3	Epicypher	14–1048
Epicypher's library preparation kit v1.1	Epicypher	14-1001 and 14-1002
Direct-zol™ RNA MiniPrep Kits	Zymogen	R2052
High-Capacity RNA-to-cDNA Kit	Applied Biosystems	4388950
PowerUp SYBR Green Master Mix for qPCR	Applied Biosystems	A25742
Deposited data		
RNA-seq, ATAC-seq and CUT&RUN fastq data and processed files	GEO: GSE281165	N/A
Experimental models: Cell lines		
HK2 cells	ATCC	CRL-2190
UOK109	Clark et al.[19]	N/A
UOK109 NONO::TFE3:eGFP KI	this paper	N/A
UOK109 KO	this paper	N/A
KO rescued with NONO::TFE3^{R}	this paper	N/A
KO rescued with NONOΔCCD::TFE3^{R}	this paper	N/A

REAGENT or RESOURCE	SOURCE	IDENTIFIER
KO rescued with NONOmut:TFE3^{R}	this paper	N/A
KO rescued with SFPQ::TFE3^{R}	this paper	N/A
KO rescued with SFPQΔCCD::TFE3^{R}	this paper	N/A
KO rescued with TFE3^{R}	this paper	N/A
UOK145	Anglard et al.[18]	N/A
FU-UR-1	Ishiguro et al.[58]	N/A
FU-UR-2	Ishiguro et al.[59]	N/A
Flp-In T-REx 293 cells	Sebastian et al.[60]	N/A
Flp-In T-REx 293 cells TFE3:eGFP	this paper	N/A
Flp-In T-REx 293 cells SFPQ::TFE3:eGFP	this paper	N/A
Flp-In T-REx 293 cells SFPQΔCCD::TFE3:eGFP	this paper	N/A
Flp-In T-REx 293 cells NONO::TFE3:eGFP	this paper	N/A
Flp-In T-REx 293 cells NONOΔCCD::TFE3:eGFP	this paper	N/A
HEK293T	ATCC	CRL-3216
U-2 OS	ATCC	HTB-96
ACHN	ATCC	CRL-1611
Experimental models: Organisms/strains		
6–8 week-old NOD scid gamma (NSG mice)	Animal Research Service, Johns Hopkins University	6–8 week-old NOD scid gamma (NSG mice)
Oligonucleotides		
Human NEAT1 with Quasar 570 Dye	Biosearch Technologies	ISMF-2037-1
Human GPNMB intron with Quasar 670 Dye	Biosearch Technologies	Custom against intron 1
Human ACTB intron for iceFISH	Biosearch Technologies	ISMF-2002-5
PCR primers	this paper	Table S3
Recombinant DNA		
pcDNA5TM/FRT/TO-Flag vector	a gift from Dr. Michael Matunis	N/A
pcDNA5TM/FRT/TO-Flag vector TFE3:eGFP	this paper	N/A
pcDNA5TM/FRT/TO-Flag vector SFPQ::TFE3:eGFP	this paper	N/A
pcDNA5TM/FRT/TO-Flag vector SFPQΔCCD::TFE3:eGFP	this paper	N/A
pcDNA5TM/FRT/TO-Flag vector NONO::TFE3:eGFP	this paper	N/A
pcDNA5TM/FRT/TO-Flag vector NONOΔCCD::TFE3:eGFP	this paper	N/A
pcDNA3.1(+)-C-eGFP vector SFPQ::TFE3:eGFP	this paper; Genscript	N/A
pcDNA3.1(+)-C-eGFP vector SFPQΔRRMs:TFE3:eGFP	this paper; Genscript	N/A
pcDNA3.1(+)-C-eGFP vector SFPQΔRRM1:TFE3:eGFP	this paper; Genscript	N/A
pcDNA3.1(+)-C-eGFP vector SFPQΔRRM2:TFE3:eGFP	this paper; Genscript	N/A
pcDNA3.1(+)-C-eGFP vector SFPQΔPLD::TFE3:eGFP	this paper; Genscript	N/A
pcDNA3.1(+)-C-eGFP vector SFPQΔCCD::TFE3:eGFP	this paper; Genscript	N/A
pcDNA3.1(+)-C-eGFP vector NONO::TFE3:eGFP	this paper; Genscript	N/A
pcDNA3.1(+)-C-eGFP vector NONOΔRRMs:TFE3:eGFP	this paper; Genscript	N/A
pcDNA3.1(+)-C-eGFP vector NONOΔRRM1:TFE3:eGFP	this paper; Genscript	N/A
pcDNA3.1(+)-C-eGFP vector NONOΔRRM2:TFE3:eGFP	this paper; Genscript	N/A

REAGENT or RESOURCE	SOURCE	IDENTIFIER
pcDNA3.1(+)-C-eGFP vector NONOΔPLD::TFE3:eGFP	this paper; Genscript	N/A
pcDNA3.1(+)-C-eGFP vector NONOΔCCD::TFE3:eGFP	this paper; Genscript	N/A
pcDNA3.1(+)-C-eGFP vector NONOmut:TFE3:eGFP	this paper; Genscript	N/A
3xFLAG::HaloTag:NONO::TFE3	this paper	N/A
3xFLAG::HaloTag:NONOΔCCD::TFE3	this paper	N/A
3xFLAG::HaloTag:NONOmut:TFE3	this paper	N/A
3xFLAG::HaloTag:SFPQ::TFE3	this paper	N/A
3xFLAG::HaloTag:SFPQΔCCD::TFE3	this paper	N/A
3xFLAG::HaloTag:TFE3	this paper	N/A
pSpCas9(BB)-2A-GFP (PX458)	Addgene	#48138
pTFE3-donor	Addgene	#112377
pTFE3.1.0-gDNA	Addgene	#112473
pEGFP-N1-TFE3	Addgene	#38120
pHIV-EGFP lentiviral vector	Addgene	#21373
pMDLg/pRRE	Addgene	#12251
pRSV-Rev	Addgene	#12253
pMD2.G	Addgene	#12259
Software and algorithms		
Zeiss Zen software	Zeiss	N/A
Nikon NIS-Elements software	Nikon	N/A
GraphPad Prism 10	Dotmatics	N/A
Slimfast.m	Sergé et al.[61]	N/A
Write_4DN_SPT_format_MATLAB	https://gitlab.com/tjian-darzacq-lab/write_4dn_spt_format_matlab	N/A
saSPT	Heckert et al.[62]; https://github.com/alecheckert/saspt	N/A
FIJI	Schneider et al.[63]	N/A
CellPose	Stringer et al.[64]	N/A
CellProfiler	Stirling et al.[65]	N/A
R version 4.2.2	R Core Team[66]	N/A
fastp	Chen et al.[67,68]	N/A
Salmon	Patro et al.[69]	N/A
DESeq2	Love et al.[70]	N/A
ComplexHeatmaps	Gu et al.[71,72]	N/A
Gene Set Enrichment Analysis (GSEA)	Mootha et al.[73] and Subramanian et al.[74]	N/A
Gene Set Variation Analysis (GSVA)	Hänzelmann et al.[75]	N/A
MSigDB pathways	Liberzon et al.[76,77]	N/A
STAR v2.7.8a	Dobin et al.[78]	N/A
bwtool	Pohl et al.[79]	N/A
trackplot	Mayakonda et al.[80]	N/A
bowtie2 v2.5.2	Langmead et al.[81]	N/A

REAGENT or RESOURCE	SOURCE	IDENTIFIER
PICARD's MarkDuplicates	Broad Institute[82]	N/A
MACS2	Zhang et al.[83]	N/A
ChIPpeakAnno	Zhu[84]	N/A
deepTools v.3.5.1	Ramírez et al.[85]	N/A
ROSE pipeline	Lovén et al.[45] and Whyte et al.[86]	N/A
DeepVenn	Hulsen[87]	N/A